Universidad de La Laguna

**Facultad de Física y Matemáticas**

MASTER EN ASTROFÍSICA

TRABAJO FIN DE MASTER

# THE BINARY STAR POPULATION OF AN EXTERNAL GALAXY

Presentado por:
**José María Arroyo Polonio**

Directora: Giuseppina Battaglia
Co-director: Guillaume Thomas

Curso Académico 2021/2022

**Abstract**

Las galaxias más comunes en el Universo son las galaxias enanas, y aunque en primera instancia podríamos pensar que se tratan de sistemas simples, numerosos trabajos previos han demostrado que estos son en realidad interesantísimos sistemas de estudio. Podemos encontrar más de cien de estas galaxias particularmente cerca de nosotros, en un entorno de poco más de 1 megapársec, formando el Grupo Local, junto a nuestra galaxia, la Vía Láctea, la galaxia de Andrómeda y algunas otras galaxias mayores. Debido a esta cercanía, nuestra actual capacidad instrumental nos permite resolver estrellas individuales pertenecientes a estas galaxias enanas y, por tanto, estudiarlas con gran detalle. Comparadas con nuestra galaxia, estas tienen una metalicidad menor, una densidad menor y, la mayoría, están dominadas por estrellas más viejas, conformando así un riquísimo campo de estudio. No solo esto, sino que el modelo jerárquico de formación de galaxias las coloca como las precursoras de las galaxias mayores, siendo estás así una pieza fundamental para entender la evolución galáctica. Entre sus más estudiadas particularidades, las galaxias enanas del Grupo Local han mostrado ser los sistemas galácticos más dominados por materia oscura, debido esto a su alta dispersión de velocidades radiales para la componente estelar. Sin embargo, la presencia de sistemas binarios puede inflar esta dispersión, y justo estas galaxias enanas han mostrado fracciones de binarias diferentes a las obtenidas en la vecindad solar, siendo así estas también la primera prueba de la no universalidad de este parámetro.

Con todo esto en mente, el objetivo principal de este trabajo es calcular la fracción de binarias de la prototípica galaxia enana Sculptor. Esto nos servirá, no solo para obtener más información acerca de poblaciones estelares externas a la Vía Láctea, sino como parámetro necesario para corregir la componente introducida por sistemas binarios en la dispersión de velocidades radiales total. Más allá de esto, el programa desarrollado podrá ser utilizado para calcular la fracción de binarias de cualquier población estelar de la que se dispongan los datos necesarios. Siendo así este útil de cara a la obtención de nuevos sets de datos, como los que puede proporcionar en el futuro WEAVE, el cual tiene programado emplear parte de su tiempo de observación para este objetivo. Empleando el mismo también se tratará de obtener información acerca de la distribución de periodos, para sistemas binarios, que podemos encontrar en Sculptor, y como esta se relaciona con la fracción de binarias.

En este trabajo, se ha usado un nuevo set de datos compuesto por observaciones espectroscópicas del telescopio "Very Large Telescope" (VLT) usando el espectrómetro multi-objeto FLAMES. Este set está compuesto por exposiciones distribuidas en 12 noches entre 2003 y 2015 en las que se observaron las mismas 96 estrellas gigantes rojas. Este set de datos es homogéneo, todas las exposiciones fueron hechas con el mismo instrumento, y tiene una cobertura temporal de 12 años, siendo este así el primero con estas características de entre los encontrados para este objetivo en la literatura. Disponemos de un catálogo de velocidades, previamente obtenido al reducir los espectros. Debido a las características de este catálogo de velocidades, principalmente a que está compuesto por observaciones separadas un total de 12 años, ha sido necesario realizar una corrección por "offsets". También se han sometido a estos a un test para ver si los errores de las velocidades han sido obtenidos correctamente, así como a una comprobación de que la calibración en longitud de onda de los espectros ha sido realizada también correctamente.

Para tratar estos datos utilizaremos una metodología encontrada en la literatura y desarrollada específicamente para este propósito. Para ello tendremos que desarrollar un programa desde cero. En primer lugar, supondremos una serie de distribuciones que describen las propiedades de los sistemas binarios que esperamos encontrar en Sculptor, entre ellas está la distribución de periodos. Para la elección de estas distribuciones nos basaremos en resultados de la literatura obtenidos para la vecindad solar. Gracias a estas simularemos nuestros datos observacionales mediante el método Monte Carlo y, posteriormente, compararemos estas simulaciones con nuestros datos observacionales en el marco de la inferencia Bayesiana. Esto nos permitirá construir una distribución de probabilidad para la fracción de binarias o para cualquier conjunto de parámetros libres que queramos estudiar. La implementación de esta metodología se ha realizado mediante un programa en Python y ha sido comprobada utilizando un set de datos de la literatura para otras galaxias enanas (Draco y Ursa Minor) y viendo como los resultados coinciden.

Obtenemos así que la fracción de binarias de Sculptor es $0.62^{+0.04}_{-0.03}$ con una confianza del 68.2% suponiendo una distribución del ratio de masas entre las dos estrellas de los sistemas binarias uniforme. Para una distribución del ratio de masas normal obtenemos $f = 0.70^{+0.04}_{-0.03}$ con la misma confianza. Estos resultados son coherentes con los encontrados en la literatura pero presentan unas incertidumbres significativamente menores. También hemos encontrado que cuando restringimos el número de observaciones a un intervalo temporal menor, el programa deja de ser sensible a algunos sistemas binarios, produciendo así una fracción menor. Por tanto, set de datos con una gran cobertura temporal como este son necesarios para el cálculo de la fracción de binarias. Por otro lado, la disminución de observaciones utilizadas conlleva un aumento del error del resultado. Hemos combinado este resultado, junto con fracciones de binarias y metalicidades de otras galaxias enanas encontradas en la literatura con el objetivo de encontrar alguna relación entre estos dos parámetros, tal y como ocurre en la vecindad solar. Sin embargo, esta relación no parece ser clara para las galaxias enanas, por tanto, habrá que esperar a tener más resultados precisos para la fracción de binarias de estas. Finalmente, al dejar la distribución del periodo de los sistemas binarios como parámetro libre junto a la fracción de binarias, vemos como hay cierta degeneración en los resultados. Menos sistemas binarios con periodos más pequeños pueden producir el mismo resultado que un número mayor de sistemas binarios con periodos mayores. Debido a esta degeneración, nuestro programa junto con nuestro set de datos no puede encontrar una solución precisa para todas estas variables simultáneamente. Sin embargo, esto podría solucionarse mediante algunas mejoras a la metodología o al añadir nuevos datos al set actual en un futuro.

# Contents


**1 Introduction** **2**
- 1.1 Dwarf galaxies in the Local Group . . . 2
- 1.2 Velocity dispersion in Local Group dwarf galaxies . . . 4
- 1.3 Binary systems in LG dwarf galaxies . . . 5
- 1.4 Objective . . . 8

**2 Data** **9**
- 2.1 The Sculptor dwarf spheroidal galaxy . . . 9
- 2.2 The dataset . . . 9
- 2.3 Data selection . . . 12
- 2.4 Correction of line-of-sight velocities and uncertanities . . . 12
  - 2.4.1 Zero-point offsets . . . 13
  - 2.4.2 Wavelenght calibration test . . . 18

**3 Methodology** **19**
- 3.1 Physics of binary systems . . . 19
- 3.2 Parameter distributions . . . 21
  - 3.2.1 Intrinsic parameters . . . 21
    - 3.2.1.1 Mass of the primary . . . 21
    - 3.2.1.2 Mass ratio . . . 21
    - 3.2.1.3 Period . . . 22
    - 3.2.1.4 Eccentricity . . . 25
  - 3.2.2 Extrinsic parameters . . . 27
    - 3.2.2.1 True Anomaly . . . 27
    - 3.2.2.2 Inclination . . . 28
    - 3.2.2.3 Argument of the periastron . . . 28
- 3.3 Analysis . . . 30
  - 3.3.1 Simulated mocks . . . 30
  - 3.3.2 Bayesian analysis . . . 31

**4 Results** **33**
- 4.1 Validation of the code: application to Draco and Ursa Minor . . . 33
- 4.2 Sculptor . . . 35
  - 4.2.1 Sculptor binary fraction . . . 35
  - 4.2.2 Groups 1 and 2 versus Group 1 only . . . 37
- 4.3 Period distribution and binary fraction . . . 38

**5 Conclusions** **40**

# 1 Introduction

The objective of this work is to use multi-epoch line-of-sight velocities ($v_{los}$) from VLT/FLAMES observations to compute the binary fraction ($f$) of Sculptor, a dwarf galaxy of the Local Group (LG). In Sec. 1.1, we present the Local Group and the different kinds of dwarf galaxies we can find in it. In Sec. 1.2, we introduce the line-of-sight velocity dispersion in such galaxies. In Sec. 1.3, we talk about our knowledge regarding binary systems in the solar neighbourhood and in LG dwarf galaxies. Finally, in Sec. 1.4, we give a precise description of the objectives.

## 1.1 Dwarf galaxies in the Local Group

In the standard cosmological model ΛCDM, the Universe has a total density of $9{,}9 \cdot 10^{-30}$ gr cm$^{-3}$ [30], it is composed by Baryonic Matter (4.6 %), Dark Matter (24 %) and Dark Energy (71.4 %). Baryonic Matter is formed mostly by atoms and a negligible amount of fast moving neutrinos. The Dark Matter is likely composed of one or more species of subatomic particles that interact mostly gravitationally with ordinary matter. Dark Energy is the repulsion energy needed to explain both the flatness of the Universe and the observed expansion. Even though there have been significant efforts trying to unveil the nature of dark matter, there have been no detections yet of its particles, and its nature is still unknown. In fact, constrains on the characteristic of dark matter particles come from astrophysical observations.

Using the accurate measurements of the cosmic microwave background of the Wilkinson Microwave Anisotropy Probe (WMAP), it has been possible to determine that this Universe is flat within a 0.5 % margin of error [30]. Moreover, on very large scales, the Universe, and therefore the distribution of matter, is isotropic and homogeneous. However, if we start zooming in, some structures start to show up; in particular, we can distinguish what is called the 'cosmic web'. This is a structure formed by huge clusters of galaxies linked to each other by dense filaments of gas and dark matter, separated by cosmic voids.

On a smaller scale, one can also find aggregations of galaxies. Those with masses under $8{\cdot}10^{13}$ $M_\odot$, as recently defined by [42], are called groups. Our galaxy, the Milky Way (MW), belongs to one of them called the Local Group (LG). It was first defined by Hubble in 1936 as "a typical, small group of nebula which is isolated in the general field", an affirmation confirmed by modern data. We can see an artistic representation of the LG in Fig. 1. It is mainly composed of two big spiral galaxies that contain about 92 % of its mass, the MW and Andromeda (M31). Nevertheless, dwarf galaxies are by far the most numerous type.

The zero velocity surface of the LG, which determines which objects are gravitationally bound to it, is $R_{LG} = 1180 \pm 150$ kpc [44]. Nowadays, the number of confirmed galaxies within this radius is of 109, according to the updated catalog of [4]. However, this number is likely an underestimation, as we expect that some faint galaxies have not been discovered yet due to their very low surface brightness. In fact, the census of LG galaxies has been strongly increasing since the release of the Sloan Digital Sky Survey (SDSS), thanks to the improvement of sensitivity.

In order to distinguish between galaxies and dwarfs, we can use the working definition given by G. Tammann at a conference held at the Observatoire de Haute-Provence in 1993, a dwarf galaxy is: "A galaxy that is fainter than $M_B \geq -16$ ($M_V \geq -17$) and more spatially extended than globular clusters is a dwarf galaxy" [49]. This definition would lead us to systems with less luminosity than $10^9 L_\odot$ . Even thought we can define what a dwarf galaxy is, there is no clear separation between dwarf and larger galaxies in terms of luminosities and sizes: dwarf galaxies appear to continue the sequences formed by larger galaxies [9].

In the LG we have a relative large sample of those dwarfs. They can be studied in great detail from samples of individual stars, obtaining even their internal dynamics. As we will see in Sec. 1.2,

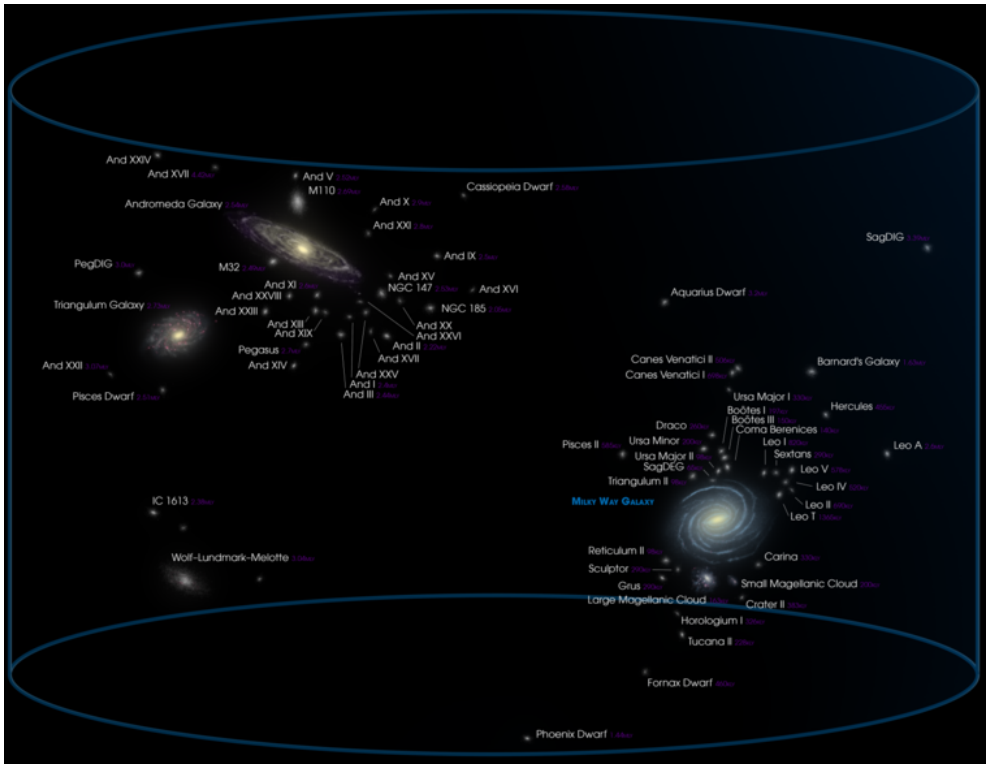


Figure 1: Representation of the Local Group made by Andrew Z. Colvin for Wikimedia Commons. [52]

the line-of-sight velocity dispersion of the stellar component of these galaxies ($\sigma_{los}$) suggests that they have very large dark-to-luminous matter ratios. This has made them of high interest to test different dark matter theories [29, 17]. Furthermore, dwarf galaxies are also much more metal-poor, less dense and more dominated by old stars, compared to the MW and M31. Therefore, we can use them to study parameters such as the binary fraction as a function of metallicity, star density, age, etc. In particular, as we will see in Sec. 1.3, the binary fraction is an important parameter for the determination of the dark matter content in dwarf galaxies. Finally, hierarchical models suggest that dwarf galaxies are building blocks of larger galaxies. In fact, there is considerable evidence of interactions between some LG dwarfs and large galaxies, which may shed some light on galaxy evolution theories [41, 27].

In terms of nomenclature, we can divide LG dwarf galaxies in:

- The "classical" dwarf galaxies can be defined as those discovered before the advent of SDSS. Therefore, they are among the brightest ones. They have been classified by their morphology mainly as dwarf spheroidals (dSphs), dwarf ellipticals (dEs) or dwarf irregulars (dIrrs). The three types have similar properties, and the most notorious difference is that, while we can find star formation in dIs, there is no gas to form stars in dsphs and dEs. They have a central surface brightness around $20 < \Sigma_0 < 27$ mag/arcsec$^2$ [9], an absolute magnitude $-9 < M_v < -17$ mag [9], and a projected half-light radius $1.8 < \log(R_{1/2}[\mathrm{pc}]) < 3$ [9].

- The recent discovered ultra-faint dwarfs (UFDs), have the faintest central surface brightness ($26 < \Sigma_0 < 30$ mag/arcsec$^2$) [23] and absolute magnitude ($-7.7 < M_v < -1$) [23] ever measured in dwarf galaxies. However, they extend to a radius comparable to classicals [23]. Due to their low surface brightnesses, they have been all discovered after the advent of SDSS.

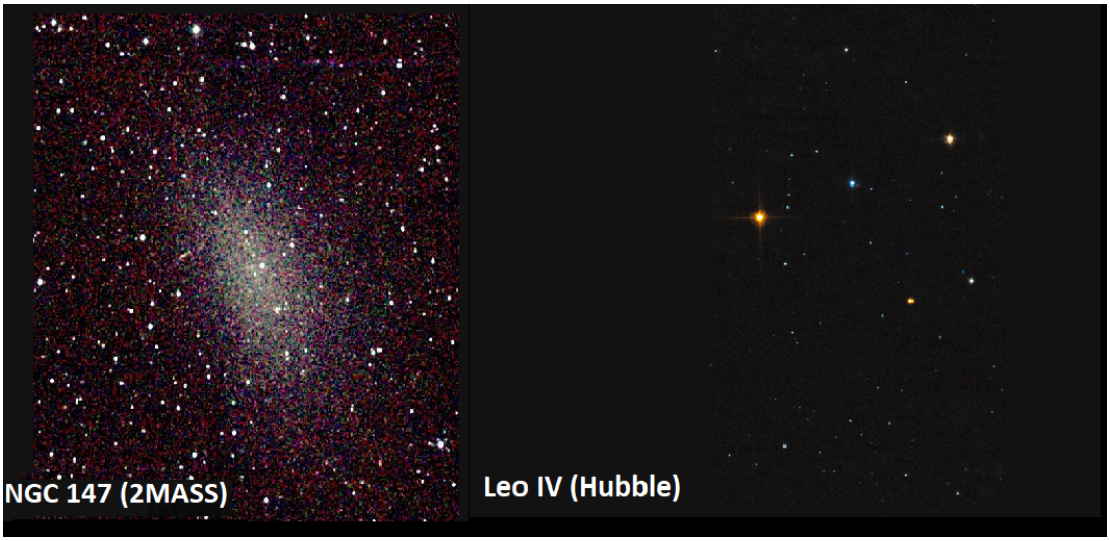


Figure 2: Example of a classical dwarf galaxy (left) and a UFD (right). Images from Two Microns All Sky Survey (2MASS) and Hubble Space Telescope.

> These dwarfs are so faint that they have even challenged the definition of galaxy itself. This term has been redefined recently (2012) by [5]: "A galaxy is a gravitationally bound collection of stars whose dynamical properties cannot be explained by a combination of baryons and Newton's laws of gravity". With this definition, we can differentiate between collection of stars with dark matter (galaxies) and without dark matter (star clusters).

Most of the classical dwarfs and UFDs are concentrated nearby the two spirals galaxies (MW and M31) as we can see in Fig 1. However, there are also some isolated members that are not bound to them, which turn out to be most of the dwarf irregulars of the LG [44, 45]. We can see an example of each type in Fig. 2.

### 1.2 Velocity dispersion in Local Group dwarf galaxies

One of the most interesting parameters of dwarf galaxies is the dynamical mass-to-light ratio, this is the ratio between the mass derived from the dynamics of the galaxy and its luminosity. Since it is quite constant for stellar populations without dark matter around $(M/L_V)_\odot = 2$ [20], it is used as an indicator of the ratio of dark-to-luminous matter. In galaxies maintained by dynamical pressure, that do not have gas, and whose stellar component has a negligible amount of rotation, like dSphs and UFDs, the dynamical mass-to-light ratio can be obtained from the stellar velocity dispersion along the line-of-sight ($\sigma_{los}$). Draco was the first dwarf galaxy with precise velocity measurements: the $v_{los}$ of 3 C-type stars was measured with an accuracy of $\pm 1$ km$\cdot s^{-1}$ [26]. Using the data from these stars, the $\sigma_{los}$ was estimated to be $6,5$ km $\cdot$ s$^{-1}$. Despite the small sample size, the results were conclusive enough to indicate a dynamical mass-to-light ratio at least an order of magnitude larger than that of the typical globular cluster (at a 95 % confidence level) [26].

Since these early observations, the velocity dispersion of many more LG dwarf galaxies, some close to the MW or M31 and some isolated ones, has been measured with much larger spectroscopic samples of accurate $v_{los}$. It is found that $\sigma_{los}$ in LG dwarf galaxies ranges from $1{,}70^{+0,50}_{-0,50}$ km$\cdot s^{-1}$[16] for Sagittarius II to $23{,}20^{+1,20}_{-1,20}$ km$\cdot s^{-1}$ [16] for NGC 6822. For dwarfs in the LG it has been found that the $\sigma_{los}$ decreases slower than expected, from the mass of the stellar component, with the absolute magnitude. Consequentially, when computing the dynamical mass-to-light ratio for those

galaxies, it is found to increase exponentially with the absolute magnitude (see Fig 10 of [4]). For the classical dSphs this implies a mass-to-light ratio up to $(M/L_V)_\odot \gtrsim 100$ [53, 15]. Moreover, for the recently discovered UFD dynamical mass-to-light ratios of $(M/L_V)_\odot \gtrsim 1000$ [23], which are the largest values ever obtained for galaxies.

Three explanations have arisen to potentially justify these mass-to-light ratio measurements; either the stars have large atmospheric motions, or the systems are being tidally disrupted by the MW, or the stars belong to binary systems. Different studies in the literature lead to certain considerations:

- The improvement of spectrographs has allowed for the observation of fainter K-giants. Since they exhibit far less atmospheric jigger than brighter carbon stars, the explanation of atmospheric motions has been ruled out.

- Regarding the tidal disruption effect, very early simulations (1998) [38] show that the fast stellar kinematics of dSphs might be produced through repeated tidal interactions of a more massive progenitor. However, more modern simulations (2015) [18] that reproduce many detailed observed properties of given MW dSphs, as well as orbital parameters derived from Gaia data [16] suggest that, in general, it is unlikely that tidal disruption can be responsible for the measured $\sigma_{los}$.

- It is clear that the presence of binaries inflates the $\sigma_{los}$. Still, one need to quantify the scale of this effect. When it comes to dSphs with $3 < \sigma_{los} < 10.5$ km$\cdot s^{-1}$ A. W. McConnachie et al. ran Monte Carlo simulations to estimate the effect of binaries [3]. The simulation estimated the velocities of stars, assuming a binary fraction between 0.05 and 0.3. They obtained that the velocity dispersion caused to binary systems cannot explain fully the $\sigma_{los}$ measured for some dwarfs like Ursa Major I, II, Bootes I, Coma Berenices and Canes Venatici II. This means dark matter is still necessary to justify their $\sigma_{los}$. However, for other fainter galaxies such as: Segue I, II, Willman I, Bootes II, Leo IV, V and Hercules there is a non-negligible chance that the measured values of $\sigma_{los}$ may be completely due to binary systems. This probability is $\gtrsim 20\,\%$ for binary fractions of 0.3 [3]. In general, even though we cannot reproduce the values of $\sigma_{los}$ only with binary systems, their presence does affect its value, meaning we have to take them into account when computing the $\sigma_{los}$ and the mass-to-light ratio afterwards. And this requires multi-epoch radial velocity measurements that allow us to identify which stars are binaries.

In Fig. 3, taken from [32], we can see how large we expect the effect of binaries to be as a function of the velocity dispersion. The ratio between the observed velocity dispersion and the intrinsic one, $\sigma_{obs}/\sigma_{int}$, is almost of 1 for all binary fractions when $\sigma_{int} > 4$ km$\cdot$s$^{-1}$. This means that the effect of the binaries is very low compared with the intrinsic $\sigma_{los}$. However, when $\sigma_{los} < 4$ the binary fraction matters; for example, for $\sigma_{int} = 0{,}5$ km$\cdot$s$^{-1}$ we can find a difference of a factor 8 between considering a binary fraction of 0 and 1.

To sum up, in general for classical dwarfs the effect of binaries affect the dispersion of velocities and then, their dark matter content. The relevance of this effect depends on the value of $\sigma_{los}$ itself. Moreover, for UFD, the velocity dispersion that we are measuring could be completely produced by binary systems. So in this case it is crucial to measure the binary fraction.

### 1.3 Binary systems in LG dwarf galaxies

Around 50% of the stars in the solar neighborhood are in binary systems, i.e. gravitationally bound to another star and orbiting around the center of mass of the system. The term binary system was first used by William Herschel in 1802 [51], when he wrote:

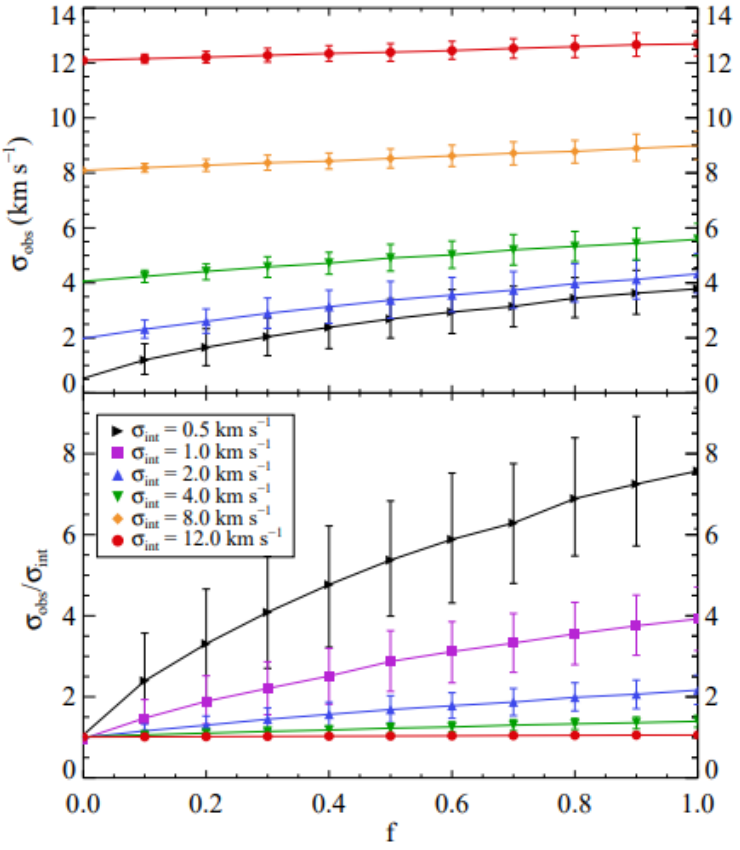


Figure 3: Relation between the velocity dispersion and the binary fraction for six mock galaxies containing 100 stars with single-epoch observations and 1km·s$^{-1}$ velocities uncertainties. The intrinsic dispersion $\sigma_{int}$ used for simulating each mock galaxy is indicated in the legend. In the upper panel we see the observed velocity dispersion $\sigma_{obs}$ and in the bottom one the ratio between $\sigma_{obs}$ and $\sigma_{int}$ as a function of the binary fraction $f$. (This figure is taken from [32])

> "If, on the contrary, two stars should really be situated very near each other, and at the same time so far insulated as not to be materially affected by the attractions of neighbouring stars, they will then compose a separate system, and remain united by the bond of their own mutual gravitation towards each other. This should be called a real double star; and any two stars that are thus mutually connected, form the binary sidereal system which we are now to consider."

However, the discovery of these systems is attributed to the amateur astronomer John Goodricke (1783), when he identified Algol as an eclipsing binary with a period of 68.8 hours.

Nowadays, due to the improvement of the instruments and to the development of new detection methods, more is known about these common systems. Thanks to new spectrographs it has been possible to obtain high-precision orbital solutions for thousands of binary systems [46, 11, 2]. Those works have derived periods, eccentricities, masses, distances, velocities and other parameters of binaries (see Sec. 3.2 for a description of these parameters). The improvement of the spatial resolution of new telescopes has allowed us to resolve individual stars in binary systems. For example, thanks to the Hubble Space Telescope, tens of visual binaries have been found in the Orion Nebula Cluster [6]; and the Kepler Mission provides nearly continuous monitoring of $\sim 156,000$ objects with an unprecedented photometric precision, allowing us to detect thousands of eclipsing binary stars [39]. This makes the study of binary systems a widely studied field nowadays.

The fraction of stars that belong to a binary system is still under discussion. Duquenoy et al. (1991) found an overall binary fraction of ~2/3 [1] for stars near the middle of the main sequence in the solar neighbourhood. However, we know that the binary fraction is a function of mass, the lower the mass of the primary (the most massive star of the binary system) is, the lower the binary fraction is. Deepak Raghavan et al. in 2010 , found that for stars in the range of $0.75 - 1 M_{\odot}$ the binary fraction is around 0.4 [7]. They also showed that the intrinsic binary fraction decreases from $f = 0.54 \pm 0.12$ near metallicities of $[M/H] = -2.7$ to $f = 0.17 \pm 0.6$ at metallicities of $[M/H] = +0.5$ for Solar-type stars. However, other studies found that metal-rich disk stars are 30% more likely to belong to a binary system with short period than metal-poor halo stars [48]. Furthermore, formation models of globular clusters can create binary fractions of 5% [22] to 100% [35]. So, in general, nowadays this variable is not well constrained.

Until recently, for most studies whose results depend on the binary fraction of the star population studied, the usual assumption was that this fraction was a universal parameter, and therefore, the same than in the solar neighbourhood. However, recent observations of stars in LG dwarf galaxies have shown that it varies. In order to be sensitive to the velocity variation induced by the orbit of stars that belongs to binary systems, we need multi-epoch data. Furthermore, in order to limit the amount of systematic errors, the different observations should be done with the same instrument, and, if possible, with the same configuration. We also require the larger signal-to-noise ratio (SNR) possible to obtain precise velocities, so we should use bright stars. Although this is not an issue for the dSphs, it is the case for the UFD, which contain only a handful of these bright stars.

In 2013, Minor [37] designed a Bayesian method to infer the binary fraction of a population of stars using multi-epoch data. He obtained the binary fraction of 4 dwarf spheroidal galaxies, Carina, Fornax, Sextans and Sculptor (see Tab. 1). In particular, his analysis inferred a binary fraction for Carina of less than 0.5 at the 90% confidence level. This is a different value than the one found in the solar neighbourhood and typically assumed also for studies of dwarf galaxies. This is the first evidence showing the assumption of a uniform binary fraction in the Universe is not valid. The data they used was obtained by using the Michigan/MIKE Fiber System (MMFS) at the Magellan/Clay Telescope at Las Campanas observatory [28]. It has a base timeline of 4 years, between 2004 and 2008, the median error of the velocities was $\pm 2.1$ km/s.

After that, Spencer et al. in 2018 [32, 33], used another Bayesian method to measure the binary

fraction of the same dwarf galaxies and of three more, Ursa Minor, Draco and Leo II (see Tab. 1). Again, more evidence of the variation of the parameter is found, for example, the binary fraction for Fornax is $0.87^{+0.12}_{-0.09}$. For this galaxy, which has a $\sigma_{los} = 10.5 \pm 1.5$ km·s$^{-1}$ [27], this large fraction would not have a big impact on the final value of $\sigma_{los}$, as we can see in Fig. 3. However, this result is quite relevant, as we can see that the binary fraction changes significantly for the different dwarfs.

For Carina, Fornax, Sextans and Sculptor the authors used the same dataset as Quinn E. Minor. For Leo II they combined four different datasets between 1995 and 2016. In those, there are a total of 9 exposures with median errors between ±1.1 and ±3 km·s$^{-1}$ for a total of 196 member stars. In the case of Ursa Minor and Draco the total dataset includes these 4 and two more in each case. One is composed of annual measurements between 1982 and 1991 where the median error in the velocity is around 1.9 km·s$^{-1}$. The other comes from observations during the years 2006 and 2011, in this case the median error is around 1.5 km·s$^{-1}$. In total, there are 284 stars for Ursa Minor and 341 for Draco. They used a heterogeneous dataset, composed by observations with different instruments and configurations and with an average of 3-4 repetitions for each star.

| Galaxy | Binary fraction [37] | Binary fraction [32, 33] |
|---|---|---|
| Draco | - | $0.50^{+0.05}_{-0.04}$ |
| Ursa Minor | - | $0.78^{+0.08}_{-0.09}$ |
| Leo II | - | $0.36^{+0.07}_{-0.08}$ |
| Carina | $0.14^{+0.28}_{-0.05}$ | $0.20^{+0.09}_{-0.013}$ |
| Fornax | $0.44^{+0.26}_{-0.12}$ | $0.87^{+0.12}_{-0.09}$ |
| Sculptor | $0.58^{+0.24}_{-0.16}$ | $0.58^{+0.15}_{-0.17}$ |
| Sextans | $0.69^{+0.19}_{-0.23}$ | $0.71^{+0.15}_{-0.14}$ |

Table 1: Binary fractions in Milky Way dSphs from studies in the literature. Col. 1 lists the galaxy name; Col. 2 the binary fraction obtained by Minor [37] and Col. 3 that obtained by Spencer et al. [32, 33].

Here, it is important to point out that to compute these binary fractions they had to assume a model for the distribution of the different parameters that influence the observed $v_{los}$ of a given binary star. In general, these distributions come from observation of binary systems in the solar neighbourhood or from theoretical models that fits those. For example, for these results Spencer et al. in 2018 [32, 33] used a log-normal distribution of periods centered in $log(P[days]) = 4.8$ and with a standard deviation of $\sigma = 2.3$, but they showed that when changing these parameters the binary fraction changes significantly, this result was also found by Minor [37] in 2013. The same result can be obtained using a lower binary fraction, and a lower value of the mean of the period distribution or a larger one for the deviation. So, since the distribution of periods is not well known in the dwarf galaxies, there is a degeneracy in the parameters.

### 1.4 Objective

In this work, we are aiming at measuring the binary fraction in the Sculptor dSph. Recently, it has been shown that this parameter varies significantly between nearby dwarf galaxies by using multi-epoch data from different observational programs. This is especially interesting if we take into account that the presence of binaries can inflate the $\sigma_{los}$ of dwarf galaxies, and therefore the dark matter content inferred. For the classical dwarfs, which typically have a $\sigma_{los} > 4$ km·s$^{-1}$, binaries could account for a maximum of around 50 % of the $\sigma_{los}$ depending on the binary fraction (see Fig. 3). However, for the recently discovered UFD, they could completely dominate it.

The objective of this work is to use unprecedented homogeneous spectroscopic data obtained with the FLAMES-GIRAFFE instrument of the VLT to compute the binary fraction of the Sculptor dSph. We have observations of 96 red giant branch stars from 12 different epochs between 2003 and 2015. In order to compute its binary fraction, we will use the Bayesian method developed by Spencer et al. [32, 33]. It consists on the construction of a likelihood function based on a set of Monte Carlo simulations mimicking the characteristics of the observations. The observational data are then used to evaluate this likelihood for different binary fractions to see which of them reproduces the best our measurements. Using this same method, we will try to set some constraints between the distribution of periods and the value of the binary fraction in dwarfs galaxies.

# 2 Data

In this section, we will introduce the dataset used in this work. In Sec. 2.1 we present the galaxy studied, the Sculptor dSph. In Sec. 2.2 we describe the observations, in Sec. 2.3 the data selection and finally, in Sec. 2.4, the correction for offsets and a robustness validation check.

## 2.1 The Sculptor dwarf spheroidal galaxy

In this work we focus on Sculptor, a classical dwarf spheroidal galaxy satellite of the Milky Way. This galaxy is located about 80 kpc away from the solar system and represents a prototypical classical dwarf galaxy. It was the first dSph galaxy to be discovered (1938) [43]. Sculptor has a half-light radius of $\log(r_{1/2}[pc]) = 1{,}97 \pm 0{,}14$ [25], an absolute magnitude of $M_V = -10{,}7 \pm 0{,}05$ [25] and a V-band central surface brightness of $23{,}7 \pm 0{,}4$ mag arcsec$^{-2}$ [27]. In Fig. 4, we can see the distribution of Gaia Early Data Release 3 (eDR3) [12, 13] sources in a ellipse of 50 arcmin around Sculptor center. In this figure, the spatial distribution is shown on the left panel and the colour-magnitude diagram (CMD) of these stars is shown on the right panel.

Concerning the star formation history of Sculptor, we can find slightly different results in the literature, M. Bettinelli et al. (2019) [24] showed that this galaxy has experienced star formation limited to the first $\sim$ 2 Gyrs after the Big Bang, and producing ~70 % of its mass. They also found that the innermost region presents the longer period of star formation, extended over ~1.5 Gyrs, and it decreases going outwards to ~0.54 Gyrs. These results suggest that in the inner part of Sculptor, the star formation continued after the reionization, and that instead, the majority of the stars were formed before or coincident with the end of it in the peripheral region. However, T. J. L. de Boer et al. (2012) [47], found that within an elliptical radius of 1 degree (1.5 kpc) the stars were formed between 14 and 7 Gyrs ago, with a peak at 13-14 Gyrs, i.e. before the recombination epoch.

Regarding the kinematics, Sculptor presents two different stellar components with different metallicities and $\sigma_{los}$, [10, 15]. The component with larger metallicity shows a $\sigma_{los}$ of $\sim 9$ kms$^{-1}$ in the center that declines to $\sim 2$ kms$^{-1}$ at a radius of 1 kpc, while the one with less metallicity shows a more constant $\sigma_{los}$ around $\sim 10$ kms$^{-1}$ [15]. This leads to a mass-to-light ratio of $158 \pm 33$ [15], making Sculptor a very dark-matter dominated galaxy.

## 2.2 The dataset

In order to tackle down the problem of the binarity in dwarf galaxies, we need not only to determine precise velocities for a large number of stars, but also a similar accuracy for the observations taken at different times. Therefore, the Very Large Telescope (VLT) was used with the multi-object high resolution spectrograph Fiber Large Array Multi Element Spectrograph (FLAMES), which is perfectly suited for this objective. It is a very stable spectrograph, it ensures reliable velocity determinations even if the observations have been taken at different times.

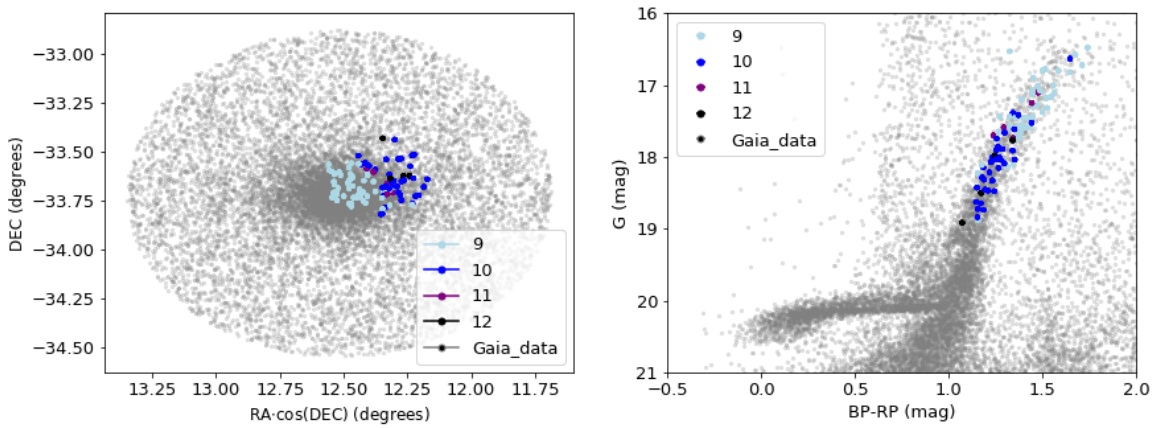


Figure 4: Distribution of Gaia eDR3 [12, 13] sources (in gray) in an ellipse of 50 arcmin around the coordinates of the Sculptor dSph, with overlaid the 96 targets of the FLAMES-GIRAFFE multi-epoch observations (large symbols.) The left panel shows the distribution on the sky and the right panel on the colour-magnitude diagram. The color indicates the number of repeated observations as indicated in the labels.

ESO's Very Large Telescope consists of four Unit Telescopes with main mirrors of 8.2 m diameter and for movable 1.8 m Auxiliary Telescopes. The multi-object spectrograph instrument FLAMES is mounted at the Nasmyth A platform of Unit Telescope 2 (UT2) and it can access targets over a field of view of 25 arcmin. This instrument has two different spectrographs: GIRAFFE a medium-high resolution spectrograph, and UVES, a high resolution one. To study the binary fraction in Sculptor, GIRAFFE is the most interesting of both, since it allows to point a large amount of stars at the same time. FLAMES/GIRAFFE was used in the MEDUSSA mode, a feeding fibre system that allow up to 132 separate objects to be observed in one go. Each fiber has an aperture of 1.2 arcsec on the sky, so it provides enough spatial resolution to resolve individual stars in a galaxy not densely populated like Sculptor. For these observations, the LR8 grating was used, with resolution around 6500, obtaining spectra in the near infrared region of the Ca II triplet at 8498 Å, 8542 Å and 8662 Å. Each observation had an exposure time of 2700 sec.

The brightest stars that we can find in dwarf galaxies without undergoing star formation are the carbon stars (C-type stars), that belong to the asymptotic giant branch. However, the number of these stars is low, and they may suffer atmospheric perturbations. Therefore, we will be observing the next most brilliant type of stars, the K-giant stars that belong to the giant branch. These have an apparent magnitude in the V-band between 20 and 16.5 in Sculptor, as we can see in Fig. 4.

Taking all of this into account, we used a specifically ensembled data-set to target 96 red giant branch stars members to Sculptor, those coloured in Fig. 4. The on the sky distribution can be seen in the left panel and the CMD in the right one. Eight repeated observations over 2 years were made, between 2014 and 2015 with the same exact instrument and the same fiber configuration to minimize instrumental issues. The stars targeted were specifically selected to have previous observations between 2003 and 2007 with the same instrument. Pre-reduced data by ESO (bias-correction, flat-fielding and wavelength calibration) was used. The extraction of the spectra, the sky-subtraction and the determination of the velocities from the near-infrared Ca II triplet lines was performed by Mike Irwin, using the methodology presented in [19]. The observations have a mean signal-to-noise ratio (SNR) of 56 and, once the velocity was derived, and a mean velocity error of 1.4 $\mathrm{km} \cdot \mathrm{s}^{-1}$. We can see an example of the spectra used in Fig. 5, this is from an exposure taken in 2015 for a star

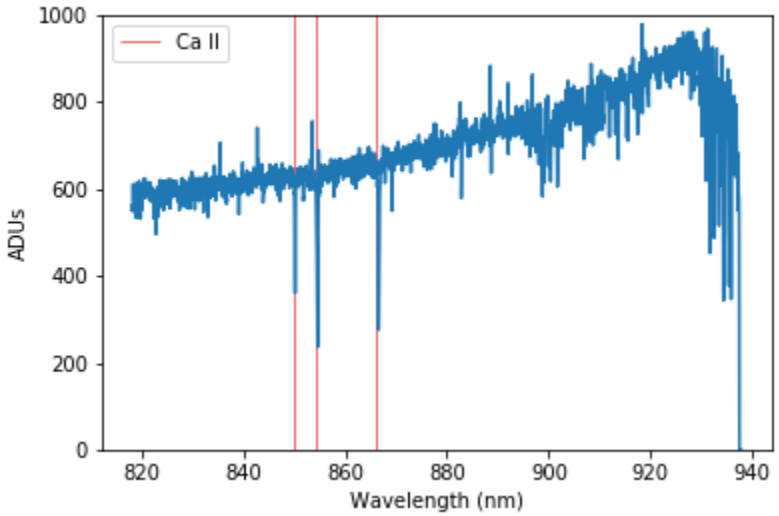


Figure 5: Spectrum of one giant red star of Sculptor with magnitude in V-band of 17.2. In red, we can find the near-infrared Ca II triplet absorption lines as indicated in the legend, used to determine the radial velocity. This spectrum has a SNR of 70.2.

with an apparent magnitude in V-band of 17.2, this particular spectrum has a SNR of 70.2.

To sum up, the dataset that will be used in this work is compounded by several spectroscopic observations of the Sculptor galaxy between 2003 and 2015, which give us a total time baseline (maximum time between observations) of 12 years. Those observations are divided into two main groups, 8 exposures taken between 2014 and 2015, (hereafter Group 2), and 5 exposures between 2003 and 2007 (hereafter Group 2). We can see a summary of the observation dates and the number of stars observed in Tab. 2.

| | Date | Observations |
|---|---|---|
| Group 1 | 2014-07-20 | 96 |
| | 2014-07-21 | 96 |
| | 2014-07-30 | 96 |
| | 2014-08-16 | 96 |
| | 2014-08-19 | 96 |
| | 2014-10-24 | 96 |
| | 2015-07-10 | 96 |
| | 2015-10-04 | 96 |
| Group 2 | 2003-09-29 | 128 |
| | 2003-09-30 | 58 |
| | 2004-09-10 | 100 |
| | 2005-11-08 | 138 |
| | 2007-09-16 | 62 |

Table 2: Date and number of stars observed of the whole dataset. Col. 1 lists the group of nights as explained in the text; Col. 2 the date of observation; and Col. 3 the number of stars observed.

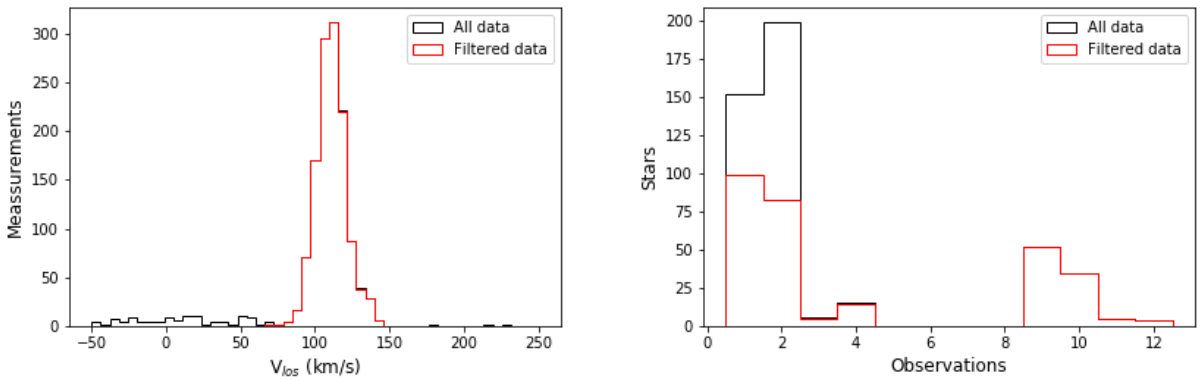


Figure 6: Distribution of our dataset, in black we can see all of it and in red the measurements that fulfill the SNR and $v_{los}$ requirements (SNR $> 5$ and 80 kms$^{-1}$ $< v_{los} <$ 140 kms$^{-1}$). The left panel shows a histogram of the velocity of measurements, and the right panel shows the number of observations per star.

## 2.3 Data selection

During those 13 nights of observations between 2003 and 2015 a total of 468 stars were observed, of which 316 have been observed at least twice. However, only 96 of them have at least 9 repeated observations, 8 from the exposures in Group 1 and at least one observation from Group 2. Regarding the rest, 199 stars have only 2 observations, and the 21 left between 3 and 4.

First, we applied some requirements to our data. In order to be sure that the stars belong to the Sculptor galaxy, which has a systemic velocity of $v_{los} = 110 \pm 0{,}5$ km·s$^{-1}$ [15] and a dispersion $\sigma_{los} = 10.1 \pm 0.3$ km·s$^{-1}$ [15], we choose a significance on velocity of $3\sigma$ ($v_{los}$ between 80 and 140 km·s$^{-1}$). We also looked for measurements good enough to obtain precise velocities (SNR $> 5$). Once the filter data this way, we obtained the distributions shown in Fig. 6. We can see that among the stars with less than 5 observations, which are all from nights of Group 2, only half accomplish the previous requirements. Nevertheless, all the stars with at least 9 observations, i.e. those observed in Group 1 and Group 2, fulfill them. Now we have the 96 stars observed in both groups, and 102 observed just in the Group 2 of nights. Even though 102 stars are more than half of our sample, we are interested in the differences between $v_{los}$, so we are looking for couples of observations of the same stars. If we take this into account, there are 182 couples of observations among those 102 stars with less than 5 observations and 3986 couples among the 96 red giant stars observed at least 9 times. That is why, if we exclude the 102 stars observed only in Group 2, made with different instrument configuration, we exclude only a 4% of our entire dataset. In view of this result, we decided to keep only the 96 red giant stars observed in both groups of nights.

Finally, we show the number of stars as a function of the time baseline for the sample of 96 stars with repeated observations in the nights of Groups 1 and 2 in Fig. 7. Our time baselines range from 8 to 12 years, which makes us sensitive to long period binary systems.

## 2.4 Correction of line-of-sight velocities and uncertainties

In Sec. 2.4.1 we quantify the zero-point offsets between observations taken at different times, and we explore the robustness of the velocity uncertainties. In Sec. 2.4.2 we look after systematic errors in the wavelength calibration.

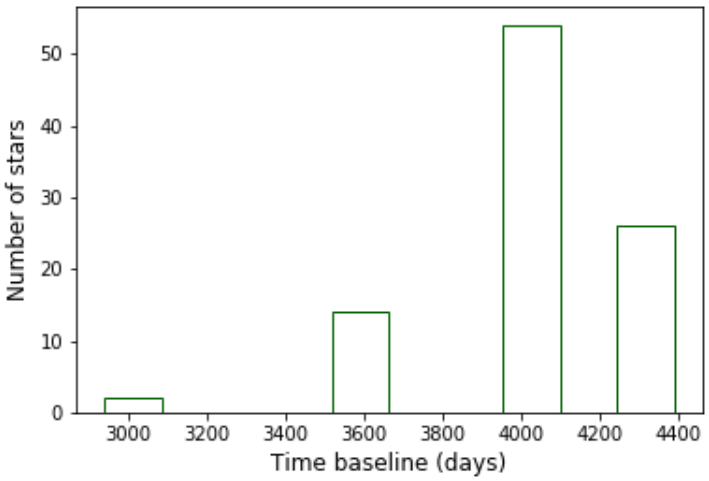


Figure 7: Number of stars versus the maximum time baseline for them in our observations, for the 96 red giant stars selected for our work.

### 2.4.1 Zero-point offsets

Even though the observations were done with the same instrument, it is still possible that systematic differences in the $v_{los}$ between the exposures taken during different nights do exist. Those systematic errors would increase the differences between the $v_{los}$ for a given star, inducing an inflated binary fraction. That is why the next step is to seek for those offsets and to correct them.

First, we take a given exposure as reference, searching for that with the best (or one of the best) SNR/magnitude relation. Considering that the catalog provided for the spectroscopic dataset did not have magnitude values of the stars observed, we did a cross-match between it and the data provided in the Gaia eDR3 [12, 13]. The cross-match was based on the declination and the right ascension that we could find in both catalogs, with a search for stars in common within 1 arcsec. Then we make sure that with this criteria, each star in our catalog was related with one and only one of the Gaia Database. We can see a representation of the relation between the SNR and the Gaia magnitude in the G-band in Fig. 8; we decided to use the date 2014-08-16 as our reference night since it seems to have one of the best overall SNR/magnitude relation.

The next step is to compare all the velocities of each star with the velocity measure during the reference night. For a single star, it is computed as $v_{ref} - v_i$, where $v_{ref}$ is the velocity measured of a given star in the reference night and $v_i$ the velocity measured during night $i$ for the same star. We can see the distribution of these differences between velocities in the left part of Fig. 9, where we have separated the nights in 3 different groups in order to better visualize the results.

We can also see the mean, the standard deviation around a mean of 0 and the scaled median absolute deviation ($sMAD$), of these difference between velocities in Tab. 3. The scaled median absolute deviation is defined as $sMAD_i = 1.48 \cdot median\,[|(v_{ref} - v_i)|]$, where $sMAD_i$ is the median absolute deviation for the night $i$. We also show the $sMAD$ for a parameter that we call $\alpha$, defined as:

$$\alpha = \frac{|v_{ref} - v_i|}{\sqrt{(\Delta v_{ref})^2 + (\Delta v_i)^2}} \tag{2.1}$$

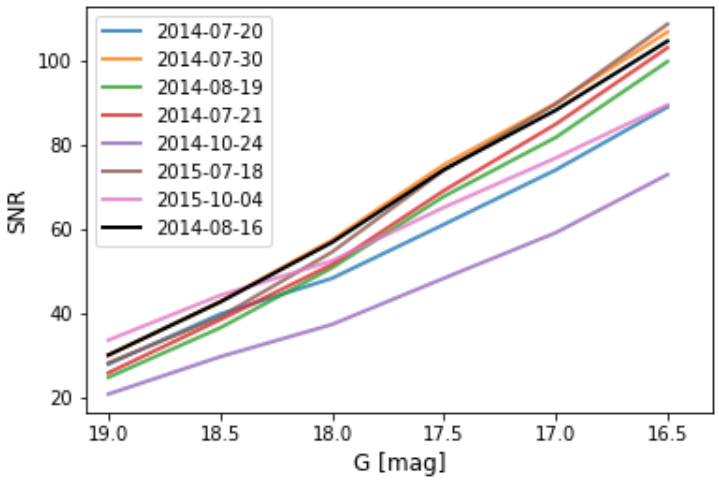


Figure 8: SNR/magnitude relation of the observed stars, each line shows the curve for each night of Group 1 as indicated in the legend. In order to make this plot easier to read, we have used bins in magnitude of 0.5 mag. The reference night (2014-05-16) is highlighted by the black curve.

where $\Delta v_{ref}$ and $\Delta v_i$ are the errors of those velocities. This is the difference between the velocity of a given night and the reference night, weighted by the errors. We will use this parameter later in this section.

| Date | $Mean$ $[\mathrm{kms}^{-1}]$ | $Stdv$ $[\mathrm{kms}^{-1}]$ | $sMAD$ $[\mathrm{kms}^{-1}]$ | $sMAD(\alpha)$ | $Obs$ |
|---|---|---|---|---|---|
| 2014-08-16 | 0 | 0 | 0 | 0 | 96 |
| 2014-07-20 | −0.05 | 2.54 | 1.49 | 0.83 | 96 |
| 2014-07-30 | 0.05 | 2.05 | 1.49 | 1.06 | 96 |
| 2014-08-19 | −0.377 | 1.98 | 1.32 | 0.81 | 96 |
| 2014-07-21 | 0.354 | 2.22 | 1.30 | 0.87 | 96 |
| 2014-10-24 | −2.11 | 3.69 | 2.96 | 0.95 | 96 |
| 2015-07-18 | 0.40 | 2.81 | 1.91 | 1.38 | 96 |
| 2015-10-04 | 0.29 | 3.94 | 2.07 | 1.21 | 96 |
| 2005-11-08 | 0.26 | 3.80 | 3.15 | 1.39 | 40 |
| 2004-09-10 | 0.93 | 3.30 | 2.03 | 1.08 | 57 |
| 2003-09-30 | 7.11 | 8.68 | 10.59 | 1.84 | 2 |
| 2003-09-29 | −0.76 | 4.34 | 2.80 | 1.19 | 50 |
| 2007-09-16 | −2.62 | 6.40 | 2.52 | 1.27 | 4 |

Table 3: Parameters of velocity difference distributions before correcting by offsets. Col. 1 lists the date of the night; Col. 2 the mean of the velocity differences; Col. 3 its standard deviation; Col. 4 lists its $sMAD$; Col. 5 lists the $sMAD$ of the parameter $\alpha$ and Col. 6 the number of stars observed.

In absence of shifts between observations taken in different nights, one expects a distribution for the difference between velocities centered on 0. However, we find some little variation in the mean, but it is mostly rather small. The first thing we have to do now is to correct for these offsets. To do this, we subtracted the mean velocity of the distribution listed in Tab.3, to the velocities of the

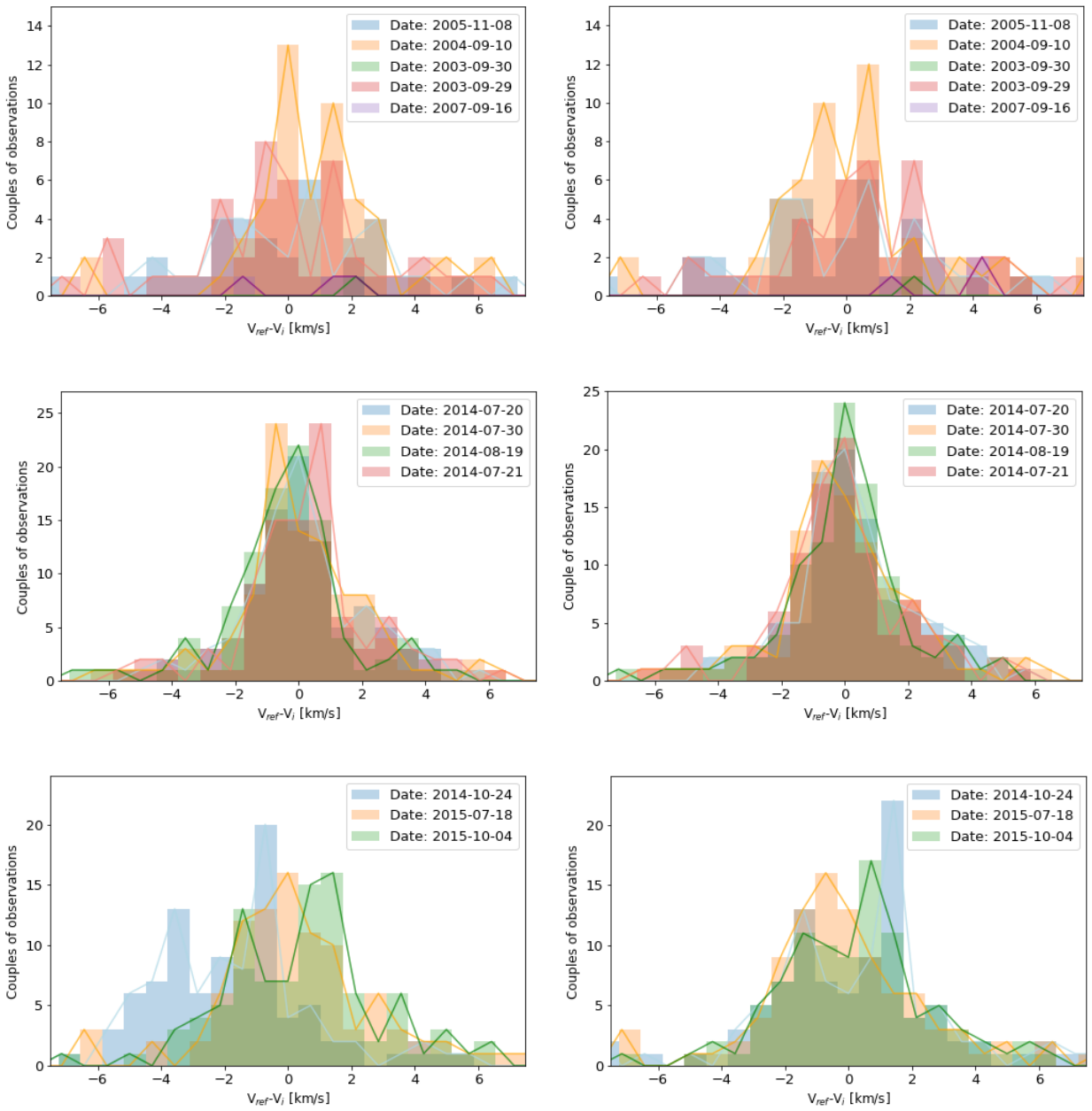


Figure 9: Histograms of the difference between velocities for the different nights, as indicated in the legend. In solid lines, we can see an interpolation between the values of the histogram with the same color for easier visualization. In the lefts panels we can see the distributions before offset correction and in the right ones after it. The 3 rows split different group of nights for visualization.

stars for each night. We can see the new distributions in the right parts of Fig. 9, and the list of the parameters in Tab. 4. Since we do not have enough statistics for the night with 2 stars, 2003-08-15, those velocities have not been corrected. We can see now that the mean of the distribution for the difference between velocities is 0 $\mathrm{kms}^{-1}$.

| Date | $Mean\ [\mathrm{kms}^{-1}]$ | $Stdv\ [\mathrm{kms}^{-1}]$ | $sMAD[\mathrm{kms}^{-1}]$ | $sMAD(\alpha)$ | Obs | $m$ | $r^2$ |
|---|---|---|---|---|---|---|---|
| 2014-08-16 | 0 | 0 | 0 | 0 | 96 | 0 | - |
| 2014-07-20 | 0 | 2.54 | 1.45 | 0.85 | 96 | -0.016 | 0.013 |
| 2014-07-30 | 0 | 2.05 | 1.49 | 1.06 | 96 | -0.027 | 0.036 |
| 2014-08-19 | 0 | 1.94 | 1.27 | 0.86 | 96 | -0.021 | 0.044 |
| 2014-07-21 | 0 | 2.19 | 1.26 | 0.89 | 96 | -0.009 | 0.0044 |
| 2014-10-24 | 0 | 3.02 | 2.36 | 0.95 | 96 | -0.02 | 0.017 |
| 2015-07-18 | 0 | 2.77 | 1.89 | 1.37 | 96 | -0.04 | 0.047 |
| 2015-10-04 | 0 | 3.93 | 2.15 | 1.20 | 96 | 0.009 | 0.0019 |
| 2005-11-08 | 0 | 3.78 | 3.15 | 1.41 | 40 | 0.006 | 0.00045 |
| 2004-09-10 | 0 | 3.16 | 1.51 | 1.08 | 57 | -0.06 | 0.041 |
| 2003-09-30 | 7.11 | 8.68 | 10.59 | 1.84 | 2 | 0.009 | 0.0015 |
| 2003-09-29 | 0 | 4.27 | 2.8 | 1.20 | 50 | -0.007 | 0.0018 |
| 2007-09-16 | 0 | 5.84 | 2.34 | 1.32 | 4 | 0.04 | 0.0018 |

Table 4: Parameters of velocity difference distributions after correcting by offsets. Col. 1 lists the date of the night; Col. 2 the mean of the velocity differences;, Col. 3 its standard deviation; Col. 4 lists its $sMAD$ ; Col. 5 lists the $sMAD$ of the parameter $\alpha$ and Col. 6 the number of stars observed. Col.7 and Col. 8 list the slope ($m$) and the dispersion coeficient ($r^2$) of the regressions from Fig. 12

In Fig. 10, we can see the histograms relatives to the parameter $\alpha$. For a set of measurements with only statistical error, we expect the distribution of differences between velocities to follow a Gaussian distribution where the width is equal to the errors. For the parameter $\alpha$, this is translated into a Gaussian centered on 0 and with standard deviation of 1, leading to a $sMAD$ of 1. So, we could use either the standard deviation or the $sMAD$ to test if our errors are well derived (the robustness of the velocity uncertainties). We will use the $sMAD$ because, we can find some values far from the mean, and this parameter does not weight the tails of the distribution that much. If the $sMAD$ is bigger than 1, it means that our errors are underestimated, and if it is smaller than 1 our errors are overestimated. In Tab.4, we can see that we obtain a $sMAD$ between 0.81 and 1.41 for the corrected nights. So, we could argue that our errors are not well obtained for some nights. However, in our particular case, we have to take into account three different particularities.

1. We are assuming that the velocities that we are measuring should be the same. Yet we expect to have some binary stars with relevant velocity variation during the nights. This effect is translated into our Gaussian distribution a little wider than they should without binary stars.

2. We have to take into account that we are using exposures of different nights separated some years. Even though we have corrected for offsets, the corrections are not perfect, they imply an error propagation. Therefore, we can expect some variation in the expected value of $sMAD$.

3. We are studying a sample of 96 points as a statistical distribution. The Central Limit Theorem establishes that around 30-50 random repetitions of a value are enough to reproduce the mean and the standard deviation of this one. So, we are not wrong when doing statistics with our sample, but we have to take into account that for a perfect Gaussian sampled with 96 points, the $sMAD$ will not be always round 1.

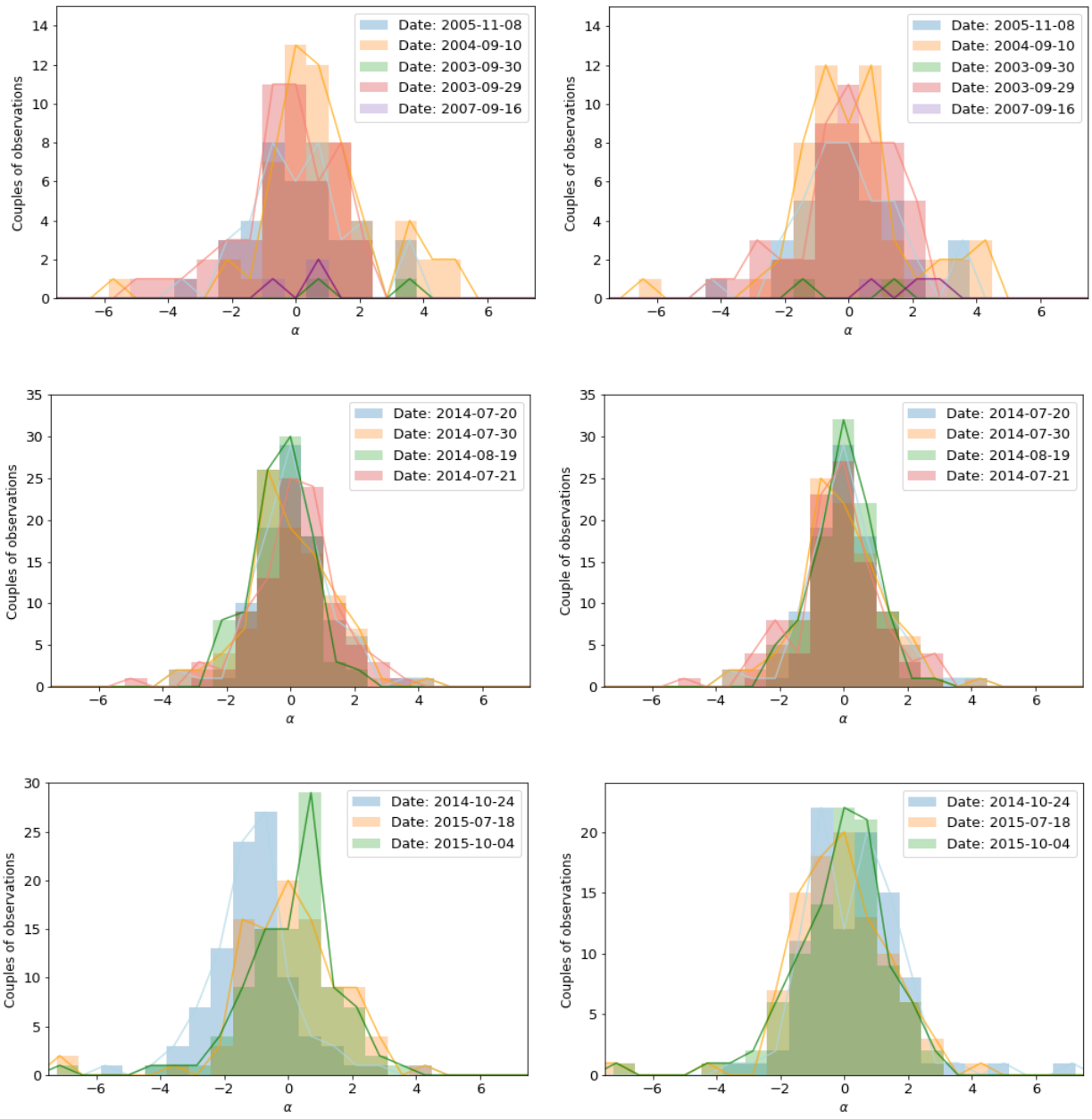


Figure 10: Histograms of the $\alpha$ parameter for the different nights, as indicated in the legend. In solid lines, we can see an interpolation between the values of the histogram with the same color for easier visualization. In the lefts panels we can see the distributions before offset correction and in the right ones after it. The 3 rows split different group of nights for visualization.

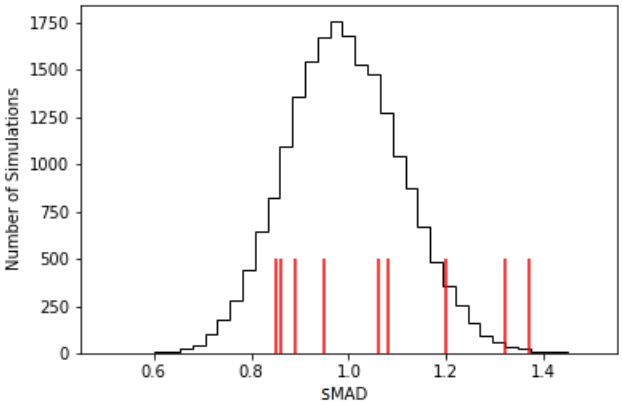


Figure 11: Histogram of the 20000 values of median absolute deviation for a normal distribution sampled with 96 points. In red, we can see the $sMAD$ values of $\alpha$ obtained for the observations after the offset correction.

Those are all reasons to justify $sMAD$ values different from 1. However, we will need only to use point 3 to prove that our values surpass this robustness test.

So, what $sMAD$ are we really expecting with our 96 point sample? In order to answer this last question and see if our errors are well determined, we decided to simulate our data using perfect Gaussian samples. So, what we did was to sample 20000 Gaussian distributions centered in 0 and with standard deviation 1 with 96 points and compute theirs $sMAD$. In Fig. 11 we can see the comparison between this distribution of 20000 samples and our data for the nights in 2014 and 2015. The value of the $sMAD$ for the date of 2003-09-30 is not included, since this night has not been corrected due to the lack of statistics. For the nights with less than 96 observations, the distribution is even wider, but since theirs $sMAD$ is so similar that they fit correctly in this one, there is no need to check for them. We can see that in general our results are not something unexpected under the conditions of the observations. The farthest point of the distribution have a value around 1.37 (for 2014-2015 nights), obtained in a night within one year to our reference night. Moreover, taking into account what we said about binaries, it is not unexpected to obtain slightly larger $sMAD$ values. In consequence, we decided that our velocity errors have been well extracted from the spectrum, so we do not have to correct them.

### 2.4.2 Wavelenght calibration test

Now we will look for some systematic error in the wavelength calibration of the spectrum. In order to trace some incoherence in the velocities, we are going to represent the parameter $\alpha$ of every measurement as a function of the $v_{ref}$ used to compute it. We can see the results in Fig. 12, the parameters of the linear fits of these distribution are shown in Col. 7 and Col. 8 of Tab. 4. We find a flat distribution with some dispersion and no relation between these two parameters. This indicates that the value of $\alpha$ is not related with $v_{ref}$, so the result of the wavelength calibration is coherent with the wavelength itself. Therefore, there is nothing to correct here.

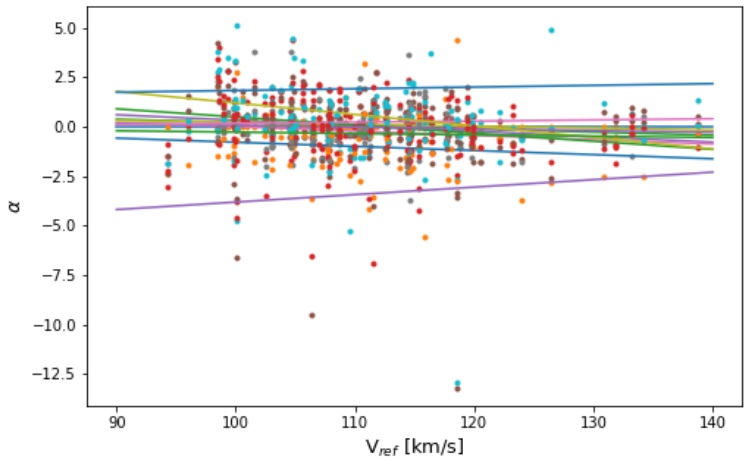


Figure 12: Value of parameter $\alpha$ as a function of $v_{ref}$. They are fitted with a linear regression just as reference, the slope and the dispersion coefficient of these regressions are listed in Tab. 4.

# 3 Methodology

In order to determine the binary fraction of the Sculptor dSph, we ran Monte Carlo simulations of the galaxy assuming different values of this parameter. The velocities of a number of stars equal to the ones observed will be simulated, i.e. 96 stars, assuming a binary fraction for the system. Then, the velocity of each star and its errors are obtained for every observation date. Afterwards, we used these data to build a likelihood function of the observational data based on these simulations, to estimate what is the binary fraction in Sculptor.

The line-of-sight velocity of a single star in a binary system depends on 7 parameters, so we need first to assume a distribution for each one. Those are the mass of the primary star $m_1$, the mass ratio between the secondary and primary star $q = m_2/m_1$, the orbital period $P$, the eccentricity $e$, the inclination $i$, the argument of the periastron $\omega$ and the true anomaly $\theta$. In the following sections, we will discuss the choice of each distribution, and then we will describe the method to compute the relative probabilities for each binary fraction value.

## 3.1 Physics of binary systems

We can study the physics of the binary systems considering the stars to be two point masses that are gravitationally bounded and isolated from interactions with other systems. Taking into account typical masses of stars and separations larger than the Roche lobe of the stars (if the separation is lower than it one star would start accreting mass from the other and the system will not be stable), we are in the case where Newtonian physics work well in order to describe trajectories, so we can use them to obtain the orbits and velocities of the stars.

The most massive star is called the primary star. It has a mass $m_1$ and it is located in the position $\overrightarrow{r_1}$, while the least massive star, called secondary star, has a mass $m_2$ and is located in $\overrightarrow{r_2}$. The separation between both stars is $r = |\overrightarrow{r_1} - \overrightarrow{r_2}|$ and each star produces a force with the same modulus and in the opposite direction acting on the other, $\overrightarrow{F}_{2\to1} = -\overrightarrow{F}_{1\to2}$, where $F = \frac{Gm_1m_2}{r^2}$ and G is the gravitational constant. Therefore, we can use the second law of Newton for each star and directly obtain the equation of motion of both stars:

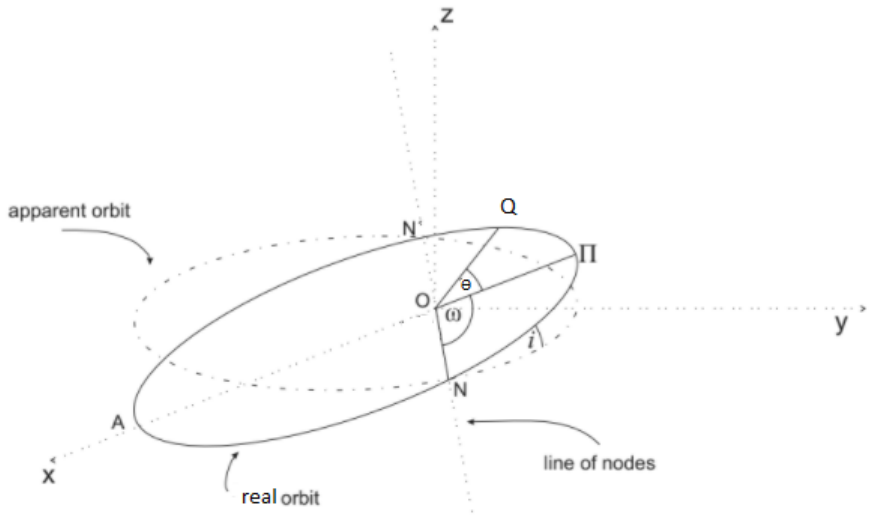


Figure 13: Real (solid line) and apparent (dashed-dotted line) orbit of a star following an elliptical orbit around the binary system's center of mass. The observer is along the z axis, defining the l.o.s. The center of mass is in O, $Q$ indicates the position of the star for a given time $t$ and finally, the apocenter $A$ and the periastron Π are given by the intersection between the real orbit and the major axis of the ellipse. We can also see the inclination as $i$, this is the angle between the apparent and the real orbit. $\omega$ is the argument of the periastron Π. Finally, $\theta$ is the true anomaly, the angle between the position $Q$ and the periastron Π. Diagram from [46].

$$m\vec{a_1} = \frac{Gm_1m_2}{r^2}\hat{r}; \quad m\vec{a_2} = \frac{Gm_1m_2}{r^2}(-\hat{r}) \tag{3.1}$$

These two equations form a system of coupled differential equations of second order that can be solved analytically.

However, we are not interested in the actual orbits of the stars, but on the velocity, particularly in the projection of the velocity along the line of sight. Before showing the solution for $v_{los}$, we have to introduce a couple of other parameters.

We can fully describe the orbit of a star in a binary system by 4 intrinsic parameters: the mass of the primary star $m_1$, the ratio between the masses $q = \frac{m_2}{m_1}$, the eccentricity of the orbit around the center of mass $e$ and the period of the orbit $P$. However, $v_{los}$ depends also on the position of the observer and the time when the star is observed (extrinsic parameters). In order to describe the relative position between the l.o.s and the observer plane we need 2 angles, and one more to indicate the time of observation, following we will describe these three extrinsic parameters. In order to visualize the trigonometry, of the system we can watch the diagram in Fig. 13: N and N' are called the ascending and descending nodes, they are located at the intersection between the real and apparent orbit, and they indicate where the star is receding and approaching the observer. $\Pi$ is the periastron, the point of the orbit that is closest to O, the furthest one is the apocenter $A$. The angle between both orbital planes, apparent and real ones, is called inclination and noted with $i$ in Fig. 13, this is one of the angles we use to describe the position. The other angle is $NO\Pi$, i.e. the argument of the periastron $\omega$. Finally, we have the angle $PO\Pi$, this is the true anomaly $\theta$, the only parameter that changes with time, it indicates the position of the star along the orbit.

Taking all these parameters into account, the line-of-sight velocity of a star in a binary system is [40]:

$$v_{los} = \frac{q\ \sin(i)}{\sqrt{1-e^2}} \left( \frac{2\pi G m_1}{P(1+q)^2} \right)^{1/3} (\cos(\theta+\omega) + e\ \cos(\omega)) \tag{3.2}$$

It is important to highlight that, if we have the distributions of the binary system intrinsic parameters in a star population, we can use this expression directly to derive the $v_{los}$ distribution of its stars.

## 3.2 Parameter distributions

There are seven parameters needed to describe a binary system. Four of them are intrinsic to the system: the mass of the primary star $m_1$, the ratio between the masses $q = \frac{m_2}{m_1}$, the period $P$ and the eccentricity of the system $e$; the other three are extrinsic, the inclination $i$, the argument of the periastron $\omega$ and the true anomaly $\theta$. In the following sections, we discuss the distribution of these parameters we used.

### 3.2.1 Intrinsic parameters

First, we will introduce the parameters intrinsic to the system. In these, we have to assume a distribution based on what we know about binary systems, mainly using distributions derived from the solar neighbourhood.

**3.2.1.1 Mass of the primary** At first sight, one could think that the correct way to reproduce the mass distribution of the stars is to use an initial mass function (IMF), assuming that the probability of two of them forming a binary system is independent of their individual mass [1]. However, the stars in our sample have not been chosen randomly. Indeed, the observation program targeted only red giant stars, so we have to reproduce their mass distribution. And these have a mass close to $0.8M_\odot$ [21] so we have decided to use a constant value of $0.8M_\odot$ for $m_1$.

**3.2.1.2 Mass ratio** For the mass ratio $q$, we will rely on the results of A. Duquenoy et al. [1], who studied the properties of G-stars that belong to binary systems in the solar neighbourhood. We can see the results that they obtained for $q$ in Fig. 14 taken from [1].

We should point out that there are a few values above 1, this basically indicates that either the primary star was bad defined or that the mass of both stars are very close, with an individual error on the stellar mass which is larger than the difference. We can also see that the curve that best fits the distribution is the dot-dashed line marked as GS. This is a mass-ratio Gaussian distribution, first derived by [36]:

$$f(q) = k\ exp\left[ \frac{-(q-\mu)^2}{2\sigma_q^2} \right], \tag{3.3}$$

where $\mu$ is the mean of the distribution, $\sigma_q$ the dispersion and $k$ a normalization factor. The authors fitted this distribution to a sample of G-dwarf stars, obtaining the values $\mu = 0.23$ , $\sigma_q = 0.42$. This will be one of the distributions we are going to adopt for $q$.

The distribution above was derived when considering all binary systems, independently on their period. However, A. Duquennoy [1] also showed that the results change when splitting the binary systems by their period (see e.g. Fig. 15). We can see that for $\log(P[\text{days}]) < 5$ the observational data is not well fitted by the Gaussian distribution GS. Therefore, we will also work with a uniform

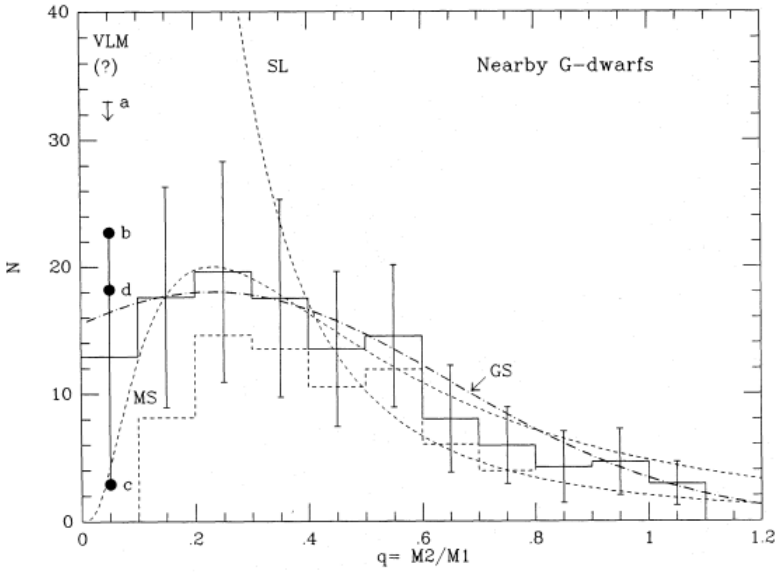


Figure 14: Distribution of the mass ratio for G-stars in the solar neighbourhood that belong to binary systems. We can see two histograms of the distribution, the dashed line is the observed one and the solid line is the one corrected for detection biases. There are different curves fitted to the corrected histogram, but we are specially interested in the one that best fit the distribution, the Gaussian curve marked as GS with a dot-dashed curve. Figure taken from [1].

mass-ratio distribution, that is quite similar to the one that we see in Fig 15. So, we can compare the results in both cases and see how dependent are the results on this choice.

The last thing we have to take into account is the lower limit, since our primary stars have a fixed mass of 0.8 $M_{\odot}$, we will establish a lower limit of q = 0.1. It corresponds to a star with a mass 0.08 $M_{\odot}$, as we do not expect stars to form below this limit since they should not have time enough to evolve and to start burning hydrogen.

Finally, we can see both distributions in Fig. 16, where we have also shown the result of the sampling method that we have used. On the technical aspect, we have used a Monte-Carlo rejection method to sample the Gaussian distribution and the function $random.uniform()$ of the *random* package of Python to generate the uniform distribution

**3.2.1.3 Period** Most of the studies about binary systems in the solar neighbourhood have shown that the observed period distribution is a log-normal function [1, 8, 34]. Therefore, we will use this distribution for our work, as explicit expressed in Equation 5:

$$f(logP) \propto exp\left(\frac{-\left(logP - \overline{logP}\right)^2}{2\sigma^2_{logP}}\right) \tag{3.4}$$

where $\overline{logP}$ is the mean of the distribution, with the period in units of days, and $\sigma_{logP}$ its width.

Previous works [32, 33, 37], have shown that the choice of these two parameter is important for the determination of the binary fraction. Therefore, we will use different realistic values for $\overline{logP}$ and $\sigma_{logP}$, to see which one of them fits better the observational data and to potentially find some constrain on them. For $\sigma_{logP}$ we will use values around 2.3, as it have been done before in the literature [33].

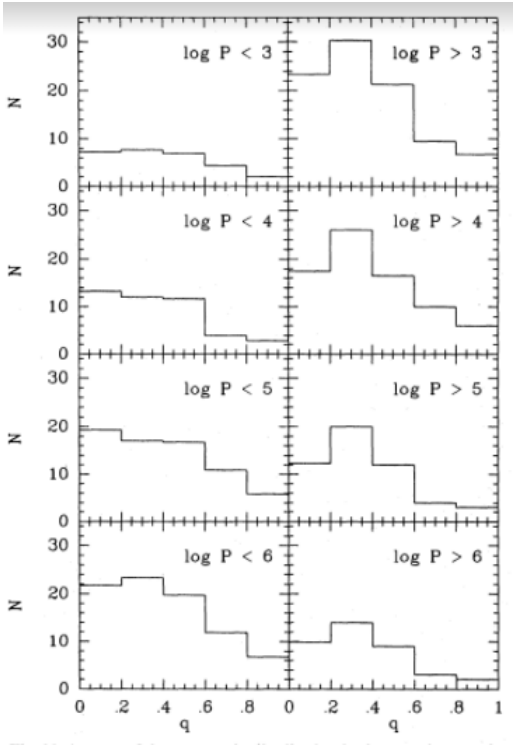


Figure 15: Observational distribution of the mass-ratio for binary systems in the solar neighbourhood for different periods separated in rows, as indicated in the legend. In the left part the distribution for periods lower than the value indicated are shown, and in the right part the one for periods larger. The logarithm of the period is in units of days. Figure taken [1]

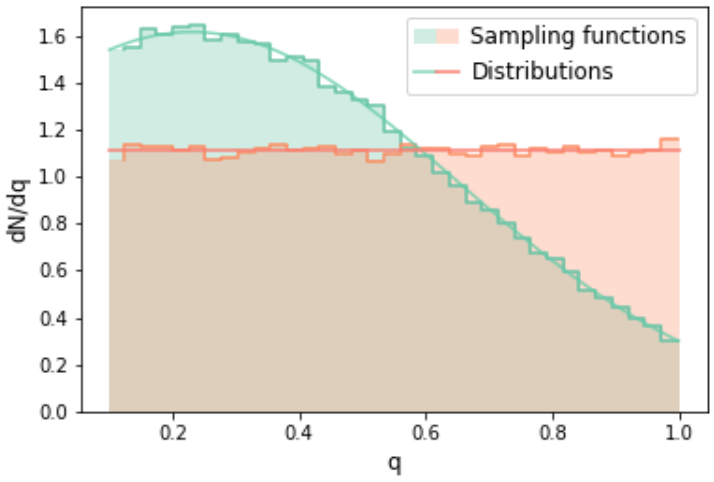


Figure 16: Distributions used for the mass ratio normalized to 1 (solid curves). The histograms are the distributions generated by the sampling function used. In green we have the one that sample the curve produced for the distribution GS and in salmon the uniform one.

Regarding the mean, we will use three different values, the first one is the intermediate one, $\overline{\log P}$[days] = 4.8 ($\approx$ 180 years). It was found by fitting the period of stars between the types F7 and G9 in the solar neighbourhood to this function [1]. In second place we will consider the results obtained when fitting K-type stars and M-dwarf stars by [8], different values of the mean between $\overline{\log P}$ [days] = 3.5 and $\overline{logP}$ [days] = 4.9, corresponding to separations of binaries between 3 and 30 AU, were found to describe the observational data. That is why we will use the smaller value as our lower limit of the mean.

Finally, we will use the population synthesis made by [34] for dwarf irregular galaxies, and the result of the fit obtained by [33] to this distribution. The value of the mean that best reproduces the period distribution of these population synthesis is $\overline{\log P}$ [days] = 5.8. This is the upper limit of the period mean that we will explore with our simulations.

We have to take into account that we are assuming that our primary star is a red giant and that we are observing a dwarf spheroidal galaxy. Therefore, there are limits in the period as a function of the limits in the semi axes of the star orbits.

On one hand, we have to notice that the lower value of the semi-minor axis permitted should be at least equal to the radius of the primary star; as it is a giant star, we will neglect the radius of the secondary. It is known by simulations and observations that the radius of these red giant stars is around 0.21 AU [33], therefore our condition is $a_{min} > 0.21$ AU. Now we can use the third law of Kepler $P^2_{min} = \frac{4\pi^2}{Gm_1(1+q)} a^3_{min}$, so we can compute the period associated to this orbit, that will be the lower one permitted; since it depends on the mass-ratio, it has to be sampled individually for every star that we simulate. In the extreme cases, we have $log\,(P_{min})\,[days] = 1.57$ for $q = 0.1$ and $log\,(P_{min})\,[days] = 1.44$ for $q = 1$.

On the other hand, we have a maximum value for the semi-major axis: it has to be such that both stars are gravitationally bound at all times. This implies that the gravitational force that one star applies on the other should be larger than the one exerted by the other nearby stars within the galaxy. We will consider that two stars are no longer bound when an interaction with another star is produced, that is to say, when the semi-major axis is larger than the mean free path of the star in the galaxy. The mean free path can be obtained as $(\pi\sigma_v t\lambda)^{-1/2}$, where $\sigma_v$ is the galaxy's velocity dispersion, $t$ is the average age of the stars and $\lambda$ is the volume number density of stars. If keep assuming that the mass of the primary star is 0.8 $M_\odot$ and either of the mass-ratio distribution shown in the previous section we obtain an average mass of around 0.4 $M_\odot$, we can use this value and the relation $L/L_\odot = \left(M/M_\odot\right)^4$ (valid for stars with masses between 0.43 and 2 $M_\odot$) to obtain the volume number density. In previous works it has been shown that the central luminosity of Sculptor is 0.055 $L_\odot/pc^3$[27], so, putting the number together we obtain that $\lambda = 2.15\ pc^{-3}$. Fit to the CMD diagram of Sculptor isochrones result in an average age of 12 Gyrs [24], and the velocity dispersion measured in our sample is 9.1 $\mathrm{km \cdot s^{-1}}$. Now we can directly substitute these numbers in the expression of the mean free path and we obtain a value for the larger semi-major axis permitted around $a_{max} = 240$ AU. As we did in the previous case, we only need to use the third law of Kepler $P^2_{max} = \frac{4\pi^2}{Gm_1(1+q)} a^3_{max}$ and obtain the limits of the period as a function of the mass-ratio. In the extreme cases, we have $log\,(P_{max})\,[days] = 6.16$ for a mass-ratio of 0.1 and $log\,(P_{max})\,[days] = 6.03$ for a mass-ratio of 1.

We implemented a Monte-Carlo rejection method to sample the distribution that we already know. The lower and upper limits of the period are established individually for each simulated stars, based on their mass ratio $q$ obtained previously. We can see both the theoretical and the sampling functions used for the two extremes cases of $q = 0.1$ and $q = 1$ in Fig 17 for the case of $\overline{logP}[days] = 4.8$ and $\sigma^2_{logP} = 2.3$.

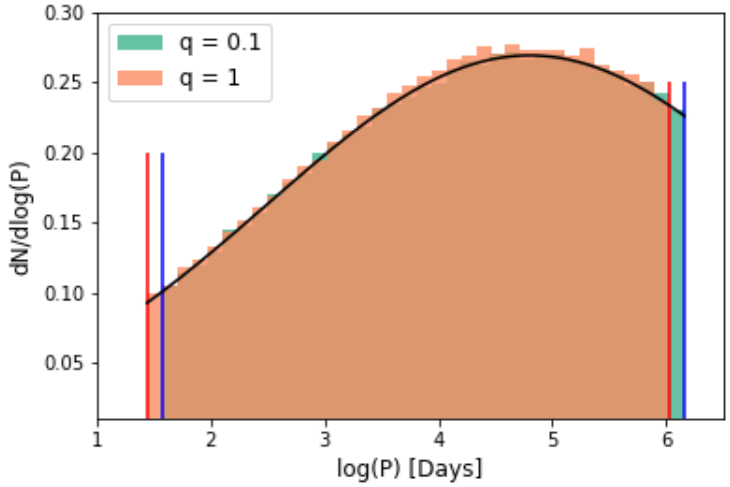


Figure 17: Period distribution for the two limit mass-ratios as indicated by the legend. The limits for each mass-ratio are plotted with vertical lines, in blue we have the limits for an extreme case of a binary system with q = 0.1, and in red for the other extreme case of q = 1. The black lines show the theoretical distribution and the colored histograms the sampling function that we have used, with the same color code as indicated for the vertical lines.

**3.2.1.4 Eccentricity** Works in the literature have shown that a relation exists between the eccentricity and the period of binary systems (see Fig. 18). Since the distribution of periods is bounded by lower and upper limits (see sect. 3.2.3), we need to take this relation into account.

In Fig. 18 we can see that the behavior of the relation between eccentricity and the period can be divided in three ranges:

- $P \lesssim 12$ days, hereafter $P_{circ}$. In this range, all the systems have e = 0, i.e. all the orbits are circular. This is due to the tidal force that occur between the stars either in the pre-main sequence or in the main sequence, so this value can be used as a tracer of the age of the system. It has been shown that the bigger this value is, the more time the stars of the population have spent in the main sequence, and then the older the population is [1].

- $P_{circ} < P < 500$ days. The binary systems in this range are called tight binaries. In Fig.18 we can see that the eccentricity is distributed around 0.3. This is the usual binaries found in open clusters.

- $P > 500$ days. In this range, the largest eccentricities are found. At first sight, it is difficult to find a relation for this range. It has been theorized that these stars should be thermalized and therefore should follow a distribution of eccentricities $f(e) = 2e$ [50]. However, it has been shown more recently that the populations of binary stars do not follow this thermal distribution [14]. Moreover, if we represent a histogram of the eccentricity distribution for the previous sample as [1] did, and we show in Fig. 19, we can see that it actually follows a uniform one.

We are interested in the eccentricity distribution of binary systems with a red giant star as a primary one. Therefore, we have to take into account that our period range is restricted, as we saw in the previous section. In fact, as we saw in Sec 3.2.3 our period distribution is not likely to have

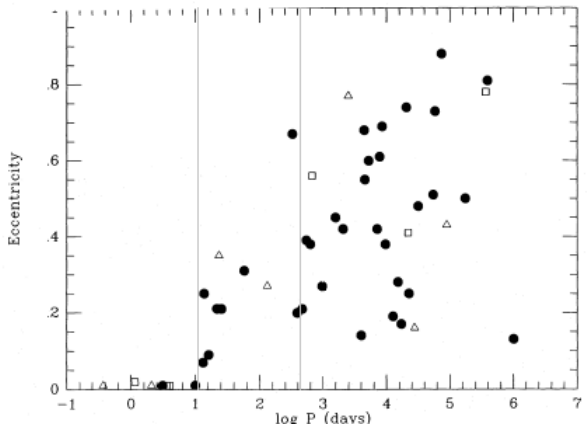


Figure 18: Period (in the x-axis) versus eccentricity (in the y-axis) for multiple systems in the solar neighbourhood. Binary systems are represented by the circles, triple systems by triangles and quadruple systems by squares. The vertical lines represent the values of 12 day and 500 days used to explain the different distributions. Fig from [1]

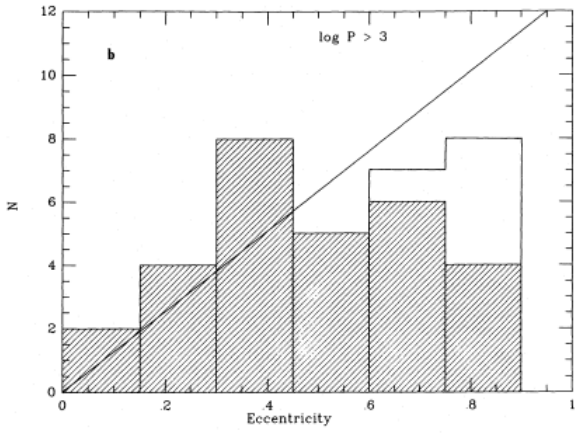


Figure 19: Histogram of the eccentricity (filled bars) of binary stars with periods $P > 1000\,\mathrm{d}$ in the solar neighbouhood. The empty bars indicate the correction due to detection errors, the last two bins have been multiplied by factors 1.2 and 2.0 respectively. Fig from [1]

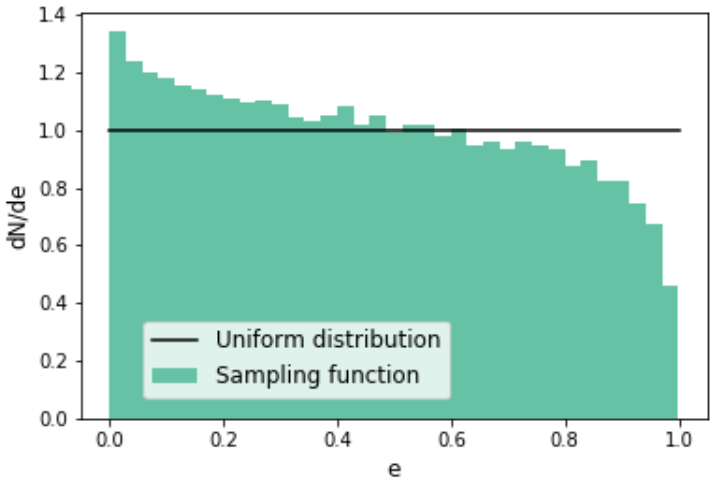


Figure 20: Eccentricity distribution; the normalized histogram produced by the sampling function that we have defined in green, and a uniform distribution as reference in black.

values below $\log P\,[days] = 2.7$, which correspond to 500 days, therefore we are mainly interested in the third range of periods ($P > 500\,d$).

Anyway, due to the evidence and as other studies did [7], we are going to choose a uniform distribution of eccentricities for binary systems with periods larger than 500 days:

$$f(e) = cte \tag{3.5}$$

Note here that there are also some restrictions. Since a certain combination of period and mass-ratio can make the stars collide for very elliptical orbits, we have to establish an upper limit. This limit of eccentricity is, as a function of the semi-minor axis $e_{max} = 1 - (a_{min}/a)$, we can compute a using the third law of Newton for a determined period and mass ratio and $a_{min}$is the lower limit for this semi-axis obtained in the previous section. So now, we need to generate a mass-ratio, then a period using the mass-ratio and then an eccentricity using both of them. We use the same Monte-Carlo rejection method as we did before to sample the distribution, whose results are shown in Fig. 20. We can see that our sampling functions rejects some large eccentricities and favor the lower ones. This is not a cut-off as it was in the period distribution because this time the limit depends on the mass-ratio and the period.

### 3.2.2 Extrinsic parameters

The extrinsic parameters are relative to the observation peculiarities of each system. We know how the distribution of these are since we can assume that the orientation of the binary systems is random because we are not a privileged observer.

**3.2.2.1 True Anomaly** The true anomaly is the first of the three extrinsic parameter that we are going to see. First of all, let's see a more precise description of this parameter in Fig. 21, where another parameter that we will need, the eccentric anomaly $E$, has been also represented.

The initial value of the true anomaly can be sampled with a uniform distribution, however, it changes with time. Moreover, it has all the time dependency as shows Equation (2). To sample this parameter, we used another auxiliary parameter called mean anomaly ($M$), it is the fraction of an

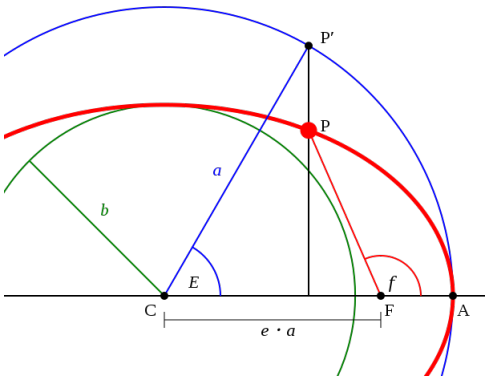


Figure 21: In red we have an elliptic orbit centered in C, we have represented two circles around this center with the radius of the semi-axes, $b$ and $a$. $P$ is the position of a star with a true anomaly $f$, and $P'$ is the vertical projection on the bigger circle, it forms an angle $E$ with the center and the semi-major axis, called eccentric anomaly. Image from Wikimedia commons [52].

elliptical orbit's period that has elapsed in a time t. So $M = M_0 + kt$, where $M_0$ is the initial mean anomaly and k is a constant, due to the second law of Kepler, as a star that have an elliptical orbit sweeps out equal areas in equal times. Thus, the parameter $k$ can be computed by using the third law of Kepler $k = \frac{2\pi}{P}$.

Now we can relate the mean anomaly of a star with its eccentric anomaly $E$ with the equation $M = E - e \cdot \sin(E)$, where $e$ is the eccentricity. We have to solve it numerically using the function $fsolve$ of the python package SciPy. Then, the true anomaly can finally be obtained with the relation $\cos(f) = \frac{\cos(E)-e}{1-e\cdot\cos(E)}$.

To sum up, we can sample the initial mean anomaly with a uniform distribution $M_0$, and then we can compute its value for all the observation times using its relation with the time. Once we have all the values for the mean anomalies in our observations, we can compute numerically the eccentric anomaly and use it to obtain the true anomaly.

**3.2.2.2 Inclination** The next extrinsic parameter is the inclination $i$. This describes the relative position between the orbital plane and the line of sight of the observer. If we do some trigonometry we can see that this distribution is a sinusoidal one, $f(i) = sin(i)$, as represented in Fig. 22. It ranges from face-on orbit, $i = 0$, to edge-on orbit, $i = \frac{\pi}{2}$, the probability of having a more edge-on orbit is more likely than a more face-on. We can understand the logic behind this behavior if we imagine an ellipse in the space. It will be face-on only to the points in a line crossing its center perpendicular to it, but edge-on to all the points of the plane that contains the ellipse itself. As done in previous sections, we use a Monte-Carlo rejection method to sample the distribution.

**3.2.2.3 Argument of the periastron** Finally, we have the argument of the periastron $\theta$. By looking at Fig. 13 it can be realized that it has to do only with the relative position of the line between the nodes and the position of the periastron. Since this orientation is random, the distribution of this parameter is a uniform distribution sampled with the function $random.uniform$ of the $random$ package of python, (see Fig. 23). It ranges from 0 to $2\pi$.

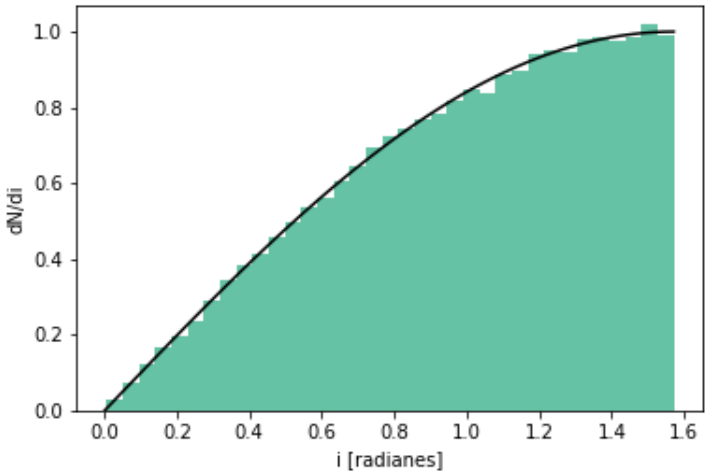


Figure 22: Distribution of the inclination. In black, we have the distribution and in green the histogram produced by the sampling function.

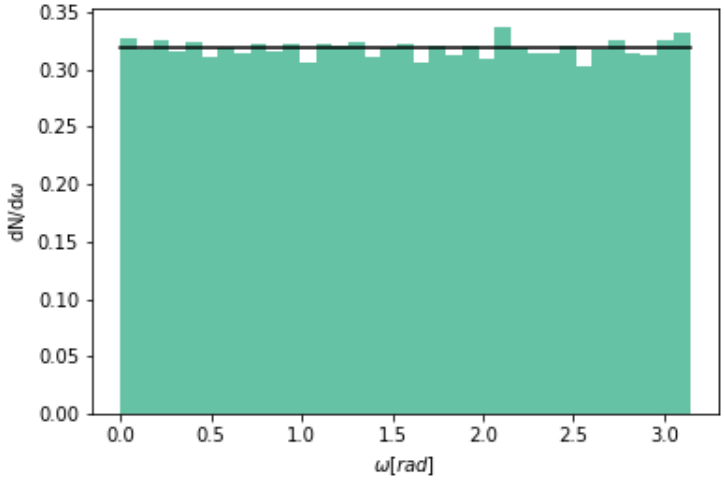


Figure 23: Distribution of the argument of the periastron. In black, we have the uniform curve and in green the histogram produced by the sampling function.

## 3.3 Analysis

Now that we know how to simulate our sample of observations, we have to find the binary fraction that better reproduces the observational data. To do so, we are going to follow the methodology developed by Spencer et al. [32, 33], implementing it into a python code.

### 3.3.1 Simulated mocks

To simulate our observations, we will follow the next steps:

1. First, we choose a binary fraction $f$. For each star observed, we randomly decide if a given star is binary or not, according to the binary fraction that we are considering. In practice, this is done by simulating a value using a uniform distribution between 0 and 1 If it is lower than $f$ it is a binary, else it is not. If it results in a binary star, we randomly assign to it a set of the 7 parameters we previously defined, again according to the selected distributions.

2. Then we compute the $v_{los}$ of the star at the time of all the observations. If the star is a binary, we use equation (2) taking into account the time evolution of the true anomaly. If the star is not a binary, we assign it a velocity of 0 $\mathrm{km \cdot s^{-1}}$.

3. Next, we compute Gaussian deviation of the velocities with a standard deviation equal to the observational error of each observation. We add this value to the one obtained in the step 2 for all observations for both, binaries and not binaries. We would like to highlight that it is not necessary to add the systemic movement of the galaxy since it would be equal for all observations and stars, and we are interested in the velocity differences.

4. Then we repeat the steps 1 to 3 for number of observed stars (96, in the case of Sculptor).

5. For statistics, we repeat the steps 1 to 4 10,000 times. Up to now, we have 10,000 different simulated mocks for a binary fraction $f$.

6. Finally, we repeat the steps 1 to 5 for all the binary fractions we are interested in. We use 100 binary fractions, equally distributed between 0 and 1. Then we group the result in pairs to eliminate random noise associated to the method.

Now we are going to define a statistical parameter that is going to be the baseline of our study, we called $\beta$, and defined as:

$$\beta = \frac{|v_i - v_j|}{\sqrt{\sigma_i^2 + \sigma_j^2}},$$

where the subscripts $i$ and $j$ denote different observations of the same star, $v$ is the measured velocity and $\sigma$ the error of this measurement. We can compute this value for both, the observed and simulated data ($\beta_{obs}$ or $\beta_{sim}$). The value of this parameter represents how large is the velocity variation between the observations, weighted by the errors.

For a star with $n$ observations, there will be $\frac{n(n-1)}{2}$ different values of $\beta$. In our particular case, we have 96 stars observed between 9 and 13 times. This results in 3986 different values of $\beta$. In previous works using this method, their observations produced 2015 $\beta$ for Draco [33], 1278 for Ursa Minor [33] and 723 for Leo II [32], far less than with our observations. The next step is to compute all the possible values of this parameter for all the data.

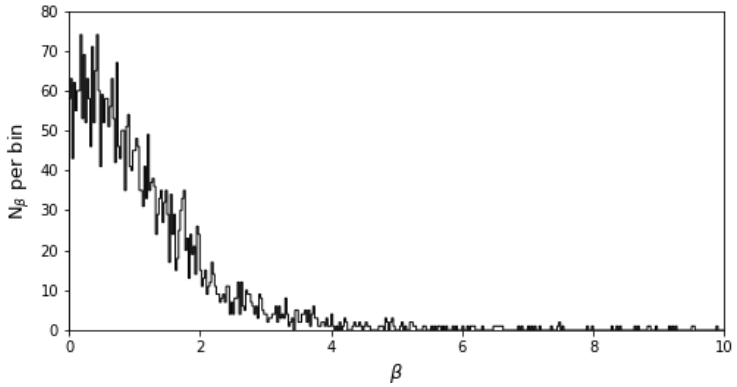


Figure 24: Distribution of observational betas computed using the VLT/FLAMES data for the Sculptor dSph. The bins have a width of 0.025.

### 3.3.2 Bayesian analysis

Now we are going to use the 10,000 simulations to build a likelihood function that describes how we expect the binaries to behave based on the distribution we explained in the previous section. Then we will evaluate this function using our observational data to obtain the posterior probability function of a given binary fraction. The Bayes theorem tells us that:

$$P\,(f\,|D,M\,) = \frac{P\,(D\,|f,M\,)\,P\,(f\,|M\,)}{P\,(D\,|M\,)},$$

where: $P\,(f\,|M\,)$ is the prior probability of a binary fraction $f$ using a model $M$. It is a uniform distribution since we do not have any prior knowledge on the binary fraction.

$P\,(D\,|f,M\,)$ is the likelihood function, it represents the probability that our observational data is well described by a fraction $f$ using a theoretical model $M$. This is the function that we have to build using the parameter $\beta$ and the 10,000 simulated mocks for every fraction $f$.

The next term, $P\,(D\,|M\,)$, is a normalization factor that we will choose so that the integral of the posterior ($P\,(f\,|D,M\,)$) probability distribution is 1.

Therefore, since $P\,(f\,|M\,)$ is uniform, the term $P\,(f\,|D,M\,)$ that represents the probability that a fraction $f$ fit well our observational data D for a theoretical model M, is directly proportional to the likelihood $P\,(D\,|f,M\,)$. Then we only need the likelihood function to obtain the posterior, and so the binary fraction probability function.

First, we are going to compute all the possible $\beta_{obs}$ of our observations. In Fig. 24 we can see a histogram that shows the distribution of this parameter for bins of 0.025 in $\beta$. We have used different values for the width of the bins, but they produce no significant variation in the results.

This is the distribution that we want to reproduce in our models. The binary fraction that best reproduces these results will be the most probable one. We are now going to see how to translate this into the Bayesian inference method. The highest value of $\beta_{obs}$ that we have is 18.12, and we are going to use bins until $\beta = 20$. We could go much higher in $\beta$, but higher bins have a negligible effect. The total number of $\beta$ that we have would be the sum of all the possible combinations of observations of the same star, $N_\beta = \sum_i n_i(n_i - 1)/2$, where $i$ indicates the star and $n_i$ is the number of observations of each. It is important to note that we have combined all our observational data so that the information about which $\beta$ corresponds to which star is lost. For notation, we are going to call the number of $\beta$ represented in the y-axis of Fig. 24, $N_i^{obs}$, where $i$ indicates the bin that corresponds to this value.

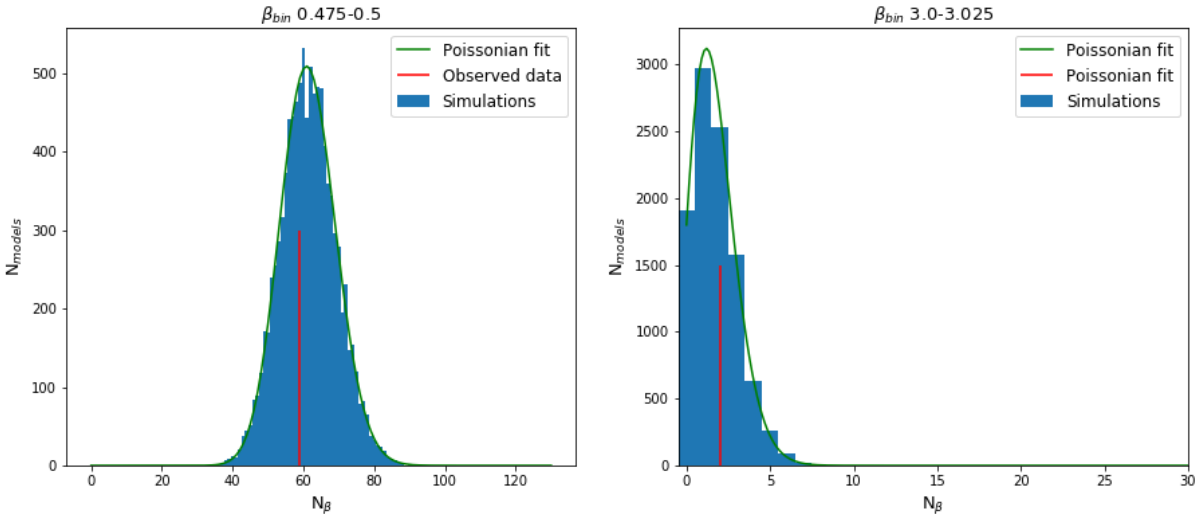


Figure 25: Histograms of the 10000 simulated values of $N_i^{sim}$: for $i = 40$, i.e. $\beta_{bin} = [0.475, 0.5]$ on the left, and for $i = 240$, i.e. $\beta_{bin} = [3.0, 3.025]$ on the right, simulated for a fraction of binaries $f = 0.5$. Since $N_i^{sim}$ is always an integer the width of the bins is 1. In red, we can see the values of $N_{40}^{obs}$ and $N_{240}^{obs}$ respectively, this is the value that we want to fit, so the closest to the center of the distribution the better this fraction reproduce the observational data. Finally, in green we can see a Poissonian function fitted to the histogram.

Next we are going to simulate our data 10000 times using the distributions described in Sec. 3.1 and the expression for the line-of-sight velocity in Eq. (2). Once we have all the velocities and their errors, we will proceed as we did for the observational data. First, we compute all the $\beta_{sim}$ for each model, and then we distribute them in 800 bins of width 0.025. The value of the y-axis in these histograms is, following the notation previously introduced, $N_i^{sim}$, where i indicates the bin that corresponds to this value. The difference now is that, since we have simulated the data, we have 10000 different values of $N_i^{sim}$ for each bin. In Fig. 25, we can see an example of those 10000 values distributed in a histogram for two different bins. All of those distributions are well fitted by a Poissonian distribution. To sum up, since we have 800 bins of $\beta$, our 10000 simulations produce 800 histograms as the ones showed in this figure, and therefore 800 Poisson distribution that fit our simulated data with the curve:

$$\phi\left(N(x) \mid \mu\right) = \frac{e^{-\mu}\mu^x}{x!} \tag{3.6}$$

where $\mu$ is the mean of the distribution and $x$ the value of $N_i$ (the x-axis of Fig. 25).

Now we can finally build our likelihood as the product of the 800 fits evaluated in the observational value $N_i^{obs}$, the one marked as red in Fig. 25:

$$P\left(f \mid D, M\right) \propto \prod_{x=1}^{800} \phi\left(N(x)_{obs} \mid \mu_{mod}\right)$$

It is easy to see that this value is a good estimator of how well our model with a fraction of binaries $f$ has described our observational data. We can see in Fig. 25 that the closer the value of $N_i^{obs}$ (red line) is to the center of the distribution, the higher the value $\phi\left(N(x)_{obs} \mid \mu_{mod}\right)$ will

| Draco | | | Ursa Minor | | |
|---|---|---|---|---|---|
| Significance | $f$(this work) | $f$(Spencer 2018[33]) | Significance | $f$ (this work) | $f$ (Spencer 2018[33]) |
| | 0.51 | 0.50 | | 0.80 | 0.78 |
| $1\sigma$ | $[-0.04, \ +0.05]$ | $[-0.04, \ +0.05]$ | $1\sigma$ | $[-0.09, \ +0.08]$ | $[-0.09, \ +0.08]$ |
| $2\sigma$ | $[-0.10, \ +0.10]$ | $[-0.10, \ +0.08]$ | $2\sigma$ | $[-0.17, \ +0.15]$ | $[-0.15, \ +0.13]$ |
| $3\sigma$ | $[-0.14, \ +0.14]$ | - | $3\sigma$ | $[-0.22, \ +0.19]$ | - |

Table 5: Values of the binary fractions of Draco (left) and Ursa Minor (right). For each table, Col. 1 lists the significance of the value; Col. 2 the result from our work and Col. 3 the results in the literature obtained by Spencer et al. (2018) [33]. In the first row of values, the result for the binary fraction is showed and in the three next rows the errors for each significance.

be, since we are just evaluating the function $\phi\left(N(x) \mid \mu\right)$. Therefore, the product of all these values represents how good the binary fraction $f$ reproduce our observational data.

Finally, we repeated this for 100 binary fractions we want between 0 and 1, and we group our result in pairs to smooth the posterior distribution, resulting in 50 values. Then, we normalized it in such a way that the integrated probability of having a binary fraction between 0 and 1 is 1, that means $\sum_f P\left(f \,|D, M\right) = 1$.

# 4 Results

In this section we will go through all the results obtained in this work. In Sec. 4.1 we are going to use the same data as Spencer et al. [33], in order to validate our implementation of their methodology by reproducing their results for the dwarfs Draco and Ursa Minor. In Sec. 4.2, we present the results for our data of Sculptor using the VLT/FLAMES dataset, in Sec. 4.2.1, we inspect the differences using our whole dataset and using only the data from the Group 1 of nights. Finally, in Sec. 4.3 we will see the results when we let the mean and sigma of the distribution of periods be free parameters.

## 4.1 Validation of the code: application to Draco and Ursa Minor

In this section, we apply the code to the same data used by Spencer et al. for the Draco and Ursa Minor dSph, in order to check the performance of our implementation of the procedure. In Fig. 26, we can see the posterior probability distribution and the cumulative one obtained for Draco and for Ursa Minor. In Tab. 5 the result for the binary fraction with confidence levels of 68.2%, 95.4% and 99.6% are listed. In both cases, a normal $q$ distribution has been used in order to compare with the results of Spencer et al. (2018) [33], since this is the distribution they used. We can see that our result match very well the ones obtained by them. The relative difference between them is of 2.5 % for Draco and of 2 % for Ursa Minor, which is within the error. This little differences probably coms from the differences between the size of the bins they used (11 different widths between 0.044 and 0.058 and averaging the result), and the one that we used (only 1 bin size of 0.025). The change of the bins width produces results so similar, here and in the rest of the results, as we checked. Moreover, we find no justification for changing the bin size as long as the distributions are well fitted to a Possionian distribution, as we also checked. Therefore, we decided to keep going with only 1 simulation for a width of 0.025.

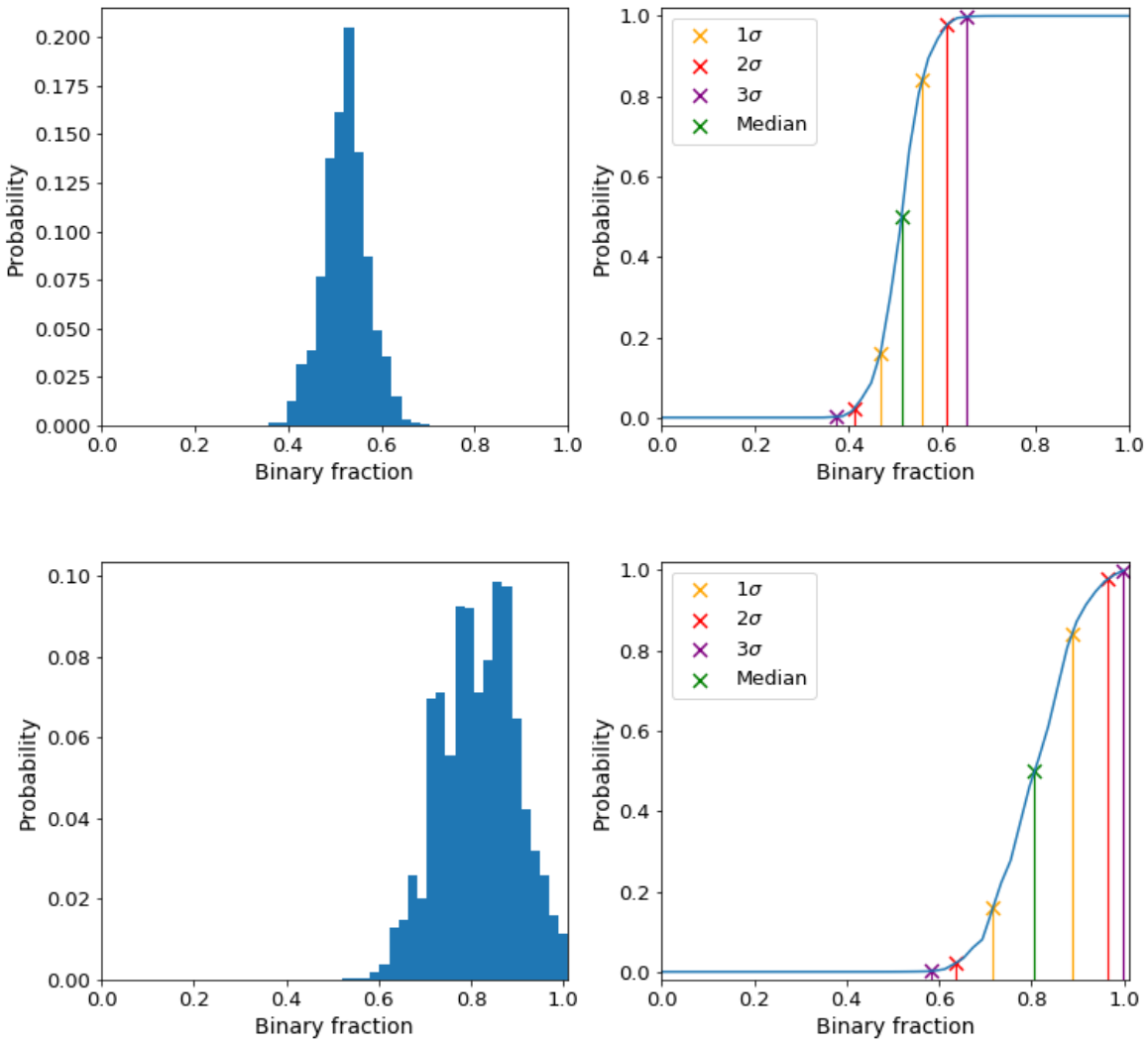


Figure 26: Probability distributions for Draco (upper row) and Ursa Minor (lower row). The left panels show the distribution of binary fractions and the right panels the cumulative distribution of the posterior. There are marks in colors, in green we can see the median of the distribution, and in orange, red and purple the intervals for $1\sigma$, $2\sigma$ and $3\sigma$ confidence levels.

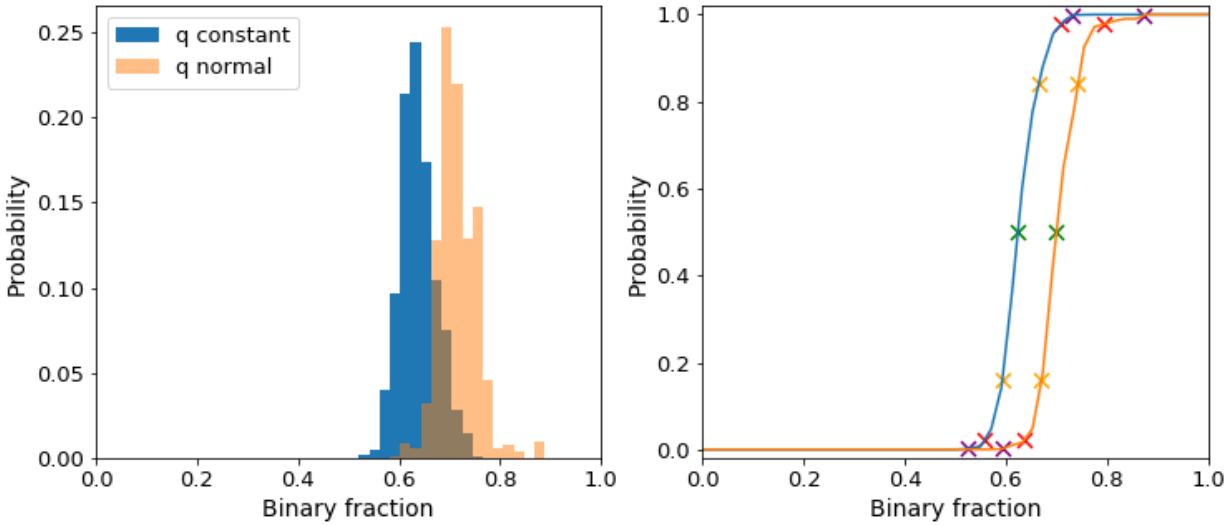


Figure 27: Left panel: Posterior distribution of binary fractions for Sculptor. Right panel: Cumulative distribution of the posterior. In blue, we can see the curves for a uniform distribution on q and in salmon for a normal distribution. There are marks in colors, in green we can see the median of the distribution, and in orange, red and purple the intervals for $1\sigma$, $2\sigma$ and $3\sigma$ confidence levels.

## 4.2 Sculptor

In Sec. 4.2.1 we will show the binary fraction probability distribution of the Sculptor dSph when using the FLAMES-GIRAFFE dataset. In Sec. 4.2.2 we compare the results between using this whole dataset and only the nights of Group 1.

### 4.2.1 Sculptor binary fraction

Here, we apply the methodology to the FLAMES-GIRAFFE dataset described in Sec. 2.2. In Fig. 27, we show the posterior and the cumulative distribution for Sculptor for a normal $q$ distribution and for a uniform one, as discussed in Sec. 3.2.1.2. In Tab. 6, the result for the binary fraction with confidence levels of 68.2%, 95.4% and 99.6% are listed. For the uniform distribution of $q$ we obtained a binary fraction of 0.62 with uncertainties of $[-0.03, +0.04]$, $[-0.06, +0.08]$ and $[-0.10, +0.11]$ respectively for each confidence level. For the normal distribution a binary fraction of 0.70 with uncertainties of $[-0.03, +0.04]$, $[-0.06, +0.09]$ and $[-0.11, +0.17]$ for each confidence level. In order to see which one of them fits better to the observational data, we compute the ratio between the integrals of the posterior probability distribution before normalize between the both cases. This is a similar method to the one used to compare binary fractions, the higher the posterior, the better the fit is. The result of this ratio was 1.03 with the uniform distribution having the higher value. However, the values are almost the same, so we cannot say that one distribution fits the data better than the other one. That is why we decided to leave both of them as possible solutions, depending on the mass ratio distribution.

We can see that our results are coherent with the ones in the bibliography from Spencer et al. (2018) [33] and Minor (2013) [37] in both cases, with differences within the errors. In the case of Spencer [33] they used a normal $q$ distribution, and Minor (2013) [37] used a combination of both, normal distribution for long period binaries and uniform one for short period binaries. Both of them

| Significance | $f$(This work, $q$ uni) | $f$(This work, $q$ normal) | $f$(Spencer 2018 [33]) | $f$(Minor 2013 [37]) |
|---|---|---|---|---|
| | 0.62 | 0.70 | 0.58 | 0.59 |
| $1\sigma$ | $[-0.03, \ +0.04]$ | $[-0.03, \ +0.04]$ | $[-0.17, \ +0.15]$ | $[-0.16, \ +0.24]$ |
| $2\sigma$ | $[-0.06, \ +0.08]$ | $[-0.06, \ +0.09]$ | - | - |
| $3\sigma$ | $[-0.10, \ +0.11]$ | $[-0.11, \ +0.17]$ | - | - |

Table 6: Values of the binary fractions for Sculptor. Col. 1 lists the significance of the value; Col. 2 the result from our work for a uniform distribution of q; Col. 3 the result from our work for a normal distribution of q Col. 4 the results in the literature obtained by Spencer et al. (2018) [33] and Col. 5 the results from Minor (2013) [37]. In the first row of values, the result for the binary fraction is showed and in the three next rows the errors for each significance.

used the same observational data from Michigan/MIKE Fiber System (MMFS) at the Magellan/Clay Telescope at Las Campanas observatory, they had 190 stars with repeated observation with a time baseline of 4 years between 2004 and 2008, the median error of the velocities was $\pm 2.1$ km/s.

Regarding the differences between the values of $f$ that we obtained for the different distributions, as Spencer et al. (2018) obtained for Draco and Ursa Minor, with the normal $q$ distribution, the value of the binary fraction is slightly larger than with the uniform one. This is because the uniform one has overall larger values for the $q$ parameter, as we can see in Fig. 16. According to Eq. (2) this is translated into larger $v_{los}$ amplitudes and therefore the fraction of binaries necessary to reproduce the observational data is lower.

If we compare the values of the binary fraction, with significance of 68.2%, obtained in Spencer et al. [33] $f = 0.58^{+0.15}_{-0.17}$, with our value for the normal $q$ distribution $f = 0.70^{+0.04}_{-0.03}$, we realize that ours is considerably larger. This is probably because they had a total time baseline of 4 years, while we have one of 12 years, this difference makes us sensitive to more binary systems, in particular the long period ones. This hypothesis will be studied in more detail in Sec 4.2.2. Moreover, we have to take into account the precision of each result, the range of values within the errors overlaps even for the significance of 68.2%, so they are not incoherent results.

Regarding the errors, we can see in Tab. 6 that our ranges are significantly smaller, we have a range of 0.07 in the $f$ for a significance of 68.2%, while Spencer obtained a range of 0.32 (4.6 times larger) and Minor one of 0.40 (5.7 times larger). In order to explain this improvement, we have to take into account two different aspects. First, their errors in velocity are larger than ours: they had a median velocity error of $\pm 2.1 \mathrm{km \cdot s^{-1}}$ and ours is of 1.4 $\mathrm{km \cdot s^{-1}}$. And second, even though they used 190 stars and we used 96, we have more repeated observations for the stars, and therefore, more statistics.

We can also compare our results with those for the solar neighbourhood. We obtain that the binary fraction of Sculptor is, with a 99.6% confidence level, above 0.52 for the $q$ uniform distribution, which gives the lower value. So, Sculptor shows, as other dwarfs galaxies, that its binary fraction is not the same as the one measured in the solar neighbourhood. This binary fraction in the solar neighbourhood is around 0.4 for stars with masses around $0.75 - 1$ $M_{\odot}$[7].

As said in Sec 1.3, relations between the metallicity and the binary fraction have been found in the solar neighbourhood. In dwarf galaxies, we have a perfect environment to test those relations, since we have low-metallicity galaxies with different binary fraction. That is why we used our result from Sculptor, those binary fractions showed in col 3. of Tab. 1 obtained by Spencer et al. 1, and the metallicities of the same dwarf galaxies obtained by [16]. As we show in Fig. 28, we cannot see a clear relation between the mean galaxy's metallicity and binary fraction, we will need to wait until having more precise measurements for the binary fraction of dwarf galaxies stellar populations.

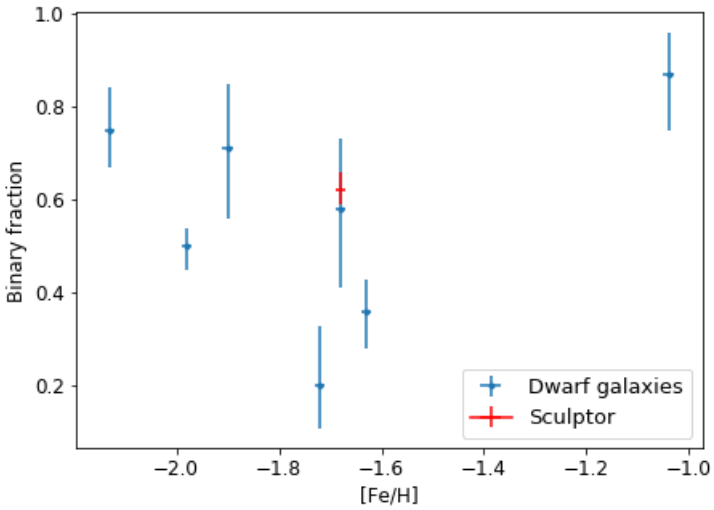


Figure 28: Relation between the metallicity and the binary fraction of nearby dSphs. In blue the binary fraction is from [33] and in red we have our result. The metallicity is from [16].

### 4.2.2 Groups 1 and 2 versus Group 1 only

At first, we can think that since the nucleus of our data set are the 8 nights from 2014-2015, when the even the same fibre configuration was used, maybe we should only use these for computing the binary fraction. That is why we decided to check how the results change between using all our data Groups 1 and 2 and only the one relative to the Group 1 of nights. In Fig. 29 we show the posterior and the cumulative distribution for Sculptor in these two cases for a uniform distribution. In Tab. 6 the result for the binary fraction for confidence levels of 68.2%, 95.4% and 99.6% are listed. As we can see, the use of Group 1 and 2 has made the distribution a bit thinner and shifted to larger values of binary fraction. Then they improve the precision of the results and makes the binary fraction slightly larger. This is because, on the one hand the more data we introduce in our program the more precise our results will be, and, on the other hand, using a sample with a bigger time baseline make us sensitive to longer period binary systems. This is the same effect we obtain when comparing our results to the ones of Spencer et al. (2018) [33] and Minor (2013) [37] in the previous section. However, the uncertainties on the binary fraction remains lower when compared to the literature studies. This is because, our velocity errors are still lower and we have not removed that much data, when we use all the nights we get 3986 values of $\beta$, and if we use only nights from 2014 and 2015 we get 2688.

| Significance | $f$ (All data) | $f$ (2014-2015 data) |
|---|---|---|
| | 0.62 | 0.56 |
| $1\sigma$ | $[-0.03, \ +0.04]$ | $[-0.04, \ +0.05]$ |
| $2\sigma$ | $[-0.06, \ +0.08]$ | $[-0.08, \ +0.10]$ |
| $3\sigma$ | $[-0.10, \ +0.11]$ | $[-0.14, \ +0.14]$ |

Table 7: Values of the binary fractions obtained by using the whole dataset (second column) and only the exposures taken between 2014 and 2015, Group 1 (third column). In the first row of values, the result for the binary fraction is shown and in the three next rows the errors for each significance.

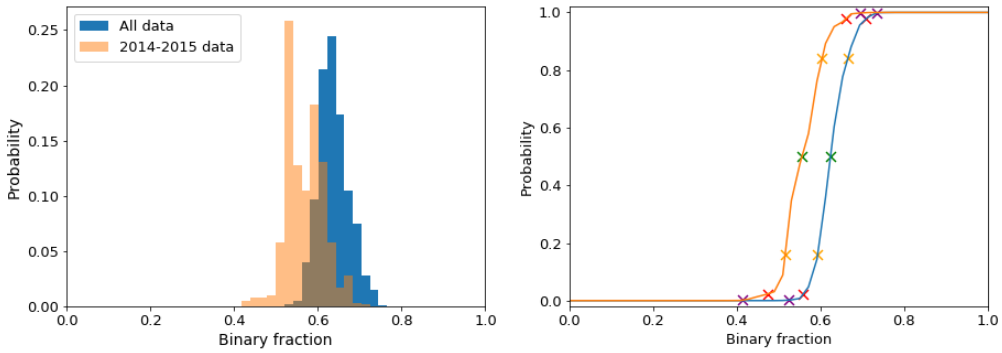


Figure 29: Left: Posterior distribution of binary fractions for Sculptor. Right: Cumulative distribution of the posterior. In blue, we can see the distributions produced by using all the data, and in salmon only using the data for the group 1 of nights.

### 4.3 Period distribution and binary fraction

In this section, we leave the mean and sigma of the period distribution as free parameters, together with the binary fraction. In particular, we are going to explore 10 values of $f$ between 0 and 1, 9 values of $\overline{logP}\,[days]$ between 3.5 and 5.8 and 9 values of $\sigma^2_{logP}$ between 1.8 and 3, all of them equally spaced. We show the posterior probability distribution obtained in Fig. 30. One can see that the degeneration mentioned in the Sec. 1.3 exists. In general, we can reproduce the same difference between velocities using lower binary fractions and lower mean periods or larger binary fractions and larger mean periods. This relation is translated also in the dispersion of the period distribution, since a larger dispersion increments the possibilities of lower periods, and those systems matter a lot in terms of contributing to large $\beta$s, so this implies lower binary fractions. This is well in lines with the results obtained by Minor (2013) [37]. If we look for the most probable case we obtain a binary fraction of $f = 0.88$, $\overline{logP}\,[days] = 5.5$ and $\sigma^2_{logP} = 1.9$, which does not seem to be a very realistic case due to the extreme values. We looked at the $\beta$ distributions produced by these values in order to rule out this case, but they really reproduce that one produced by our observational data (Fig. 24). Therefore, this will remain as a result to check and study in more detail in the future.

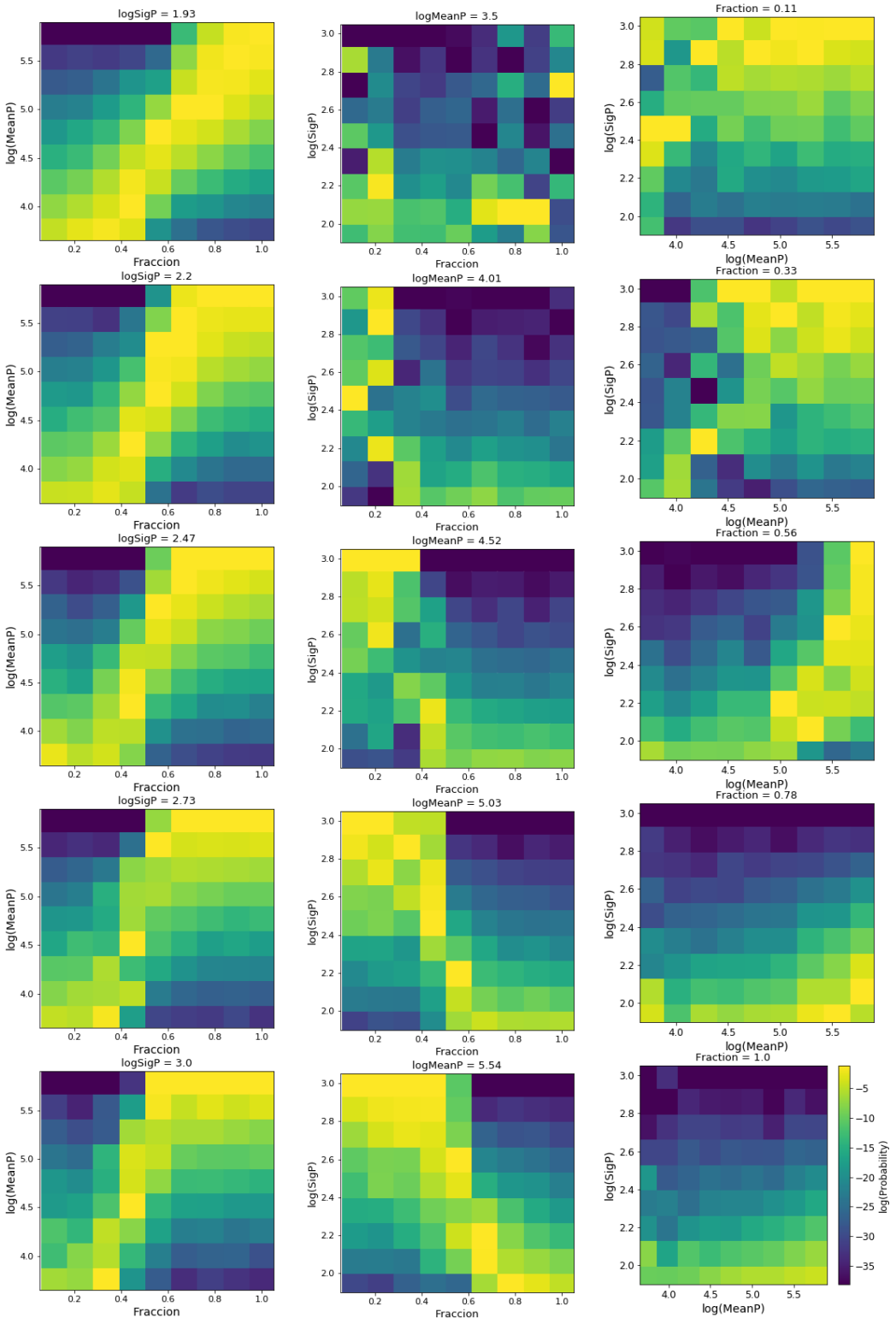


Figure 30: Posterior probability distributions obtained by exploring different values for the mean and the sigma of the period distribution. Left panels: $\overline{logP}\,[days]$ vs $f$ for different values of $\sigma^2_{logP}$ as indicated in the titles; middle panels: $\sigma^2_{logP}$ vs $f$ for different values of $\overline{logP}\,[days]$ as indicated on the titles; Right panels: $\overline{logP}\,[days]$ vs $\sigma^2_{logP}$ as indicated in the titles. All the distributions have been normalized and each color indicates the probability of that combination, as indicated in the colormap. Most likely models are indicated in yellow, less likely in blue.

# 5 Conclusions

In the LG we can find a large sample of dwarf galaxies close enough to resolve their individual stars, which allows us to study these systems in great detail. These dwarfs have shown the largest mass-to-light ratios ever measured for a galactic system, as obtained from their $\sigma_{los}$. Moreover, recently, it has been shown that the binary fraction of these galaxies is not the same as the one in the solar neighbourhood, this is important since it is a determinant parameter when computing $\sigma_{los}$. Therefore, we have reproduced a methodology developed by Spencer et al. (2018) [33, 32] to constrain the properties of the binary stars population of dwarf galaxies by using multi-epoch line-of-sight velocity measurements of red giant stars. We have applied this method to a novel VLT/FLAMES spectroscopic sample for the Sculptor dSphs, that includes repeated observations of 96 red giant branch stars with a time baseline of 12 years. We have obtained the following results:

- We have validated the implementation of the methodology by reproducing satisfactorily the results of Spencer et al. (2018) [33]. Using their same data, we have computed the binary fraction for Draco and Ursa Minor with our code. We obtained a binary fraction of $0.51^{+0.05}_{-0.04}$ (Draco) and $0.80^{+0.08}_{-0.09}$ (Ursa Minor) and they obtained $0.50^{+0.05}_{-0.04}$ and $0.78^{+0.08}_{-0.09}$ respectively. So both the median value and the errors are in accordance.

- We obtain a binary fraction for Sculptor $f = 0.62^{+0.04}_{-0.03}$ with a confidence of 68.2% if we assume a uniform distribution of $q$, or $0.70^{+0.04}_{-0.03}$ for a normal distribution, with the same confidence level. Those results are coherent with those in the literature [33, 37], but our uncertainties are much improved. This is most likely due to the homogeneity of the sample and the number of repeated observations.

- We studied how the time baseline of the sample affects the results. We saw that the results of the literature [33] were slightly lower $\left(f = 0.58^{+0.15}_{-0.17}\right)$, as their dataset presented a lower time baseline (4 years). Then we restrict our dataset by using only the 8 nights between 2014 and 2015, obtaining similar results to those showed in the literature. We find smaller binary fractions and a slightly wider range of confidence due to data lost, $f = 0.56^{+0.05}_{-0.04}$.

- Regarding the mean and sigma of the period distribution of the binary stars population in Sculptor, either our dataset or the methodology are not good enough to place strong constraints. However, we recover the expected behavior also showed in the literature.

Overall, we have built a solid code that with the correct initial distributions can compute the binary fraction not only for dwarf galaxies, but for any other population. This is specially interesting since we are continually finding more and more faint dwarfs. Even though, nowadays, we are not able to compute the binary fractions of UFD due to the difficulties of obtaining multiple exposures of many faint stars, it is necessary for the estimation of the dark matter of them, and it will be done in the future for sure. Moreover, the code can be used to simulate observations of mock galaxies. This could be helpful to optimize the distribution of nights for future observing programs, as the part of WEAVE Galactic Archeology observations aimed at obtaining the binary fraction of a sample of Milky Way dwarf spheroidals.

There are a lot of work in this field for the future:

- We expect to have more precise and numerous measurements of velocities in the Sculptor dSph. These will allow us to expand the time baseline of our sample by combining them with the ones that we already have, provided the dataset will be homogenized.

- Due to the improvement of telescopes and instruments, we also expect to apply our code to other dwarf galaxies using futures datasets. With the precision that it has shown, we could finally shed some light on the issue about of the binary fraction. Now it seems to be clear that it is not a universal parameter, but, how does it depend on the environment where the stars have formed?

- The degeneracy issue between the period distributions and the binary fractions is also a problem to be solved. We will explore what additional data need to be added to the current dataset, in order to derive more precise results and to constraint this distribution.

- This method can still to be optimized. When we apply this methodology we lose all information about which beta correspond to which star, if a star shows large betas for all the observations combinations they are probably more representative than an isolated one. Moreover, we are studying only absolute velocity variations. However, we could also use the information about the sign of the difference between velocities; this could be specially interesting when talking about period distributions.

- The code can be used for testing theories of star formation too; we could study binary populations in diffuse clusters or field populations and compare their statistical properties to that of simulations.

To sum up, thanks to the code we have done and the multi-epoch dataset used, we have obtained the most precise binary fraction for the Sculptor dSph up to date. We have also inspected the different effect of using datasets with different properties (amount of repetitions and time baseline) and different distributions for the parameters of the binary systems. Finally, it is important to note that the code derived can be used in the future with new observations for any star population to constrain any of the binary system parameters.

## References


[1] A. Duquenoy and M. Mayor,
*Multiplicity among solar-type stars in the solar neighbourhood. Distribution of the orbital elements in an unbiased sample*,
Astronomy and Astrophysics (A&A), 248, 485-524 (1991). Link

[2] Adrian M. Price-Whelan, David W. Hogg, Hans-Walter Rix et al. ,
*Close Binary Companions to APOGEE DR16 Stars: 20,000 Binary-star Systems Across the Color–Magnitude Diagram*,
The Astrophyisical Journal, 895:2, 2020 May 20. Link

[3] Alan W. McConnachie and Patrick Côté,
Revisiting the influence of unidentified binaries on velocity dispersion measurements in ultra-faint stellar system,
The Astronomical Journal letters, 2010 October 20 . 722: L209-L214. Link

[4] Alan W. McConnachie,
*The observed properties of dwarf galaxies in and around the local group*,
The Astronomical Journal, 144:4, 2012 July. Link

[5] B. Willman and J. Strader,
*"Galaxy", defined*,
The Astronomical Journal, 144:76, 2012 September. Link

[6] Bo Reipurth, Marcelo M. Guimarães et al. ,
*Visual binaries in the orion nebula cluster*,
The Astrophysicial Journal, 2007 December 134: 2272-2285. Link

[7] D. Raghavan, H. A. McAlister et al. ,
*A survey of stellar families: Multiplicity of solar-type stars*,
The Astrophysicial Journal Supplement Series, 190: 1-42, 2010 September. Link

[8] Debra A. Fischer and Geoffrey W. Marcy,
*Multiplicity among M Dwarfs*,
The Astrophysicial Journal, 396: 178-194, 1992 September 1. Link

[9] Eline Tolstoy, Vanessa Hill and Monica Tosi,
*Star Formation Histories, Abundances and Kinematics of Dwarf Galaxies in the Local Group*,
Anual Review of Astronomy & Astrophysics, vol. 47, Issue 1, pp. 371-425 September 2009. Link

[10] Eline Tolstoy,
*Detailed Studies of the Sculptor Dwarf Spheroidal Galaxy in the Milky Way halo*,
Proceedings of the International Astronomical Union, IAU Symposium, Volume 298, pp. 53-58 January 2014. Link

[11] Evgenya L. Shkolnik, Leslie Hebb et al. ,
Thirty new low-mass spectroscopic binaries,
The Astrophysicial Journal, 2010 June 20 716:1522. Link

[12] Gaia Collaboration et al. ,
*The Gaia mission* ,
Astronomy & Astrophysics 29272. September 15, 2016.Link

[13] Gaia Collaboration et al. ,
*Gaia Early Data Release 3* ,
Astronomy & Astrophysics manuscript 650, C3. September 15, 2016.Link

[14] Gasparad Duchêne and Adam Kraus,
*Stellar Multiplicity*,
Annual Review of Astronomy and Astrophysicis 2013 51. 1056-8700/97/0610-00. Link

[15] Giuseppina Battaglia, A. Helmi,
The kinematic status and mass content of the Sculptor dwarf spheroidal galaxy,
The Astronomical Journal, 2008 July 1 . 681: L13-L16. Link

[16] Giuseppina Battaglia, S. Taibi, G. F. Thomas and T. K. Fritz ,
*Gaia early DR3 systemic motions of Local Group dwarf galaxies and orbital properties with a massive Large Magellanic Cloud.* ,
Astronomy &Astrophysicis (17 Junio 2021). Link

[17] Giuseppina Battaglia, Amina Helmi, Maarten Breddels,
*Internal kinematics and dynamical models of dwarf spheroidal galaxies around the Milky Way*,
New Astronomy Reviews. Volume 57, Issues 3-4 September-October 2013, 52-79. Link

[18] Giuseppina Battaglia, Antonio Sollima and Carlo Nipoti,
*The effect of tides on the Fornax dwarf spheroidal galaxy*,
Monthly Notices of the Royal AStronomical Society, Volume 454 , 2401-2415 (2015). Link

[19] Giuseppina Battaglia, M. Irwin, E. tolstoy et al,
*Analysis and calibration of Ca II triplet spectroscopy of red giant branch stars from VLT/FLAMES observations*,
Monthly Notices of the Royal AStronomical Society, Volume 383 , 183-199 (2008). Link

[20] H. Baumgardt,
*N-body modelling of globular clusters: masses, mass-to-light ratios and intermediate-mass black holes*,
Monthly Notices of the Royal AStronomical Society, Volume 464 , 2174-2202 (2017). Link

[21] J.C Hargreaves, G. Gilmore and J. D. Annan,
*The influence of binary stars on dwarf spheroidal galaxy kinematics*,
Mon. Not. R. Astronomic Society 279, 108-120 (1996). Link

[22] Jarrod R. Hurley, Sverre J. Aarseth and Michael M. Shara,
*The core binary fractions of star clusters from realistic simulations*,
The Astrophyisical Journal, 665:1, 2007. Link

[23] Joshua D. Simon,
*The Faintest Dwarf Galaxies*,
Annual Review of Astronomy and Astrophysics. Vol. 57:375-41 (2019)Link

[24] M. Bettinelli, S. L. Hidalgo et al. ,
*The star formation history of the Sculptor dwarf spheroidal galaxy* ,
The Astronomical Journal 122(5) (August 2001). Link

[25] M. Irwin and D. Hatzidimitriou,
*Structural parameters for the Galactic dwarf spheroidals*,
Mon. Not. R. Astron. Soc. 277, 1354-1378 (1995). Link

[26] Mark Aaronson ,
*Accurate radial velocities for carbon stars in Draco and Ursa Minor: The First hint of a dwarf spheroidal mass-to-light ratio* ,
The Astronomical Journal, 1983 March . 266: L11-L15. Link

[27] Mario Mateo,
*Dwarf Galaxies of the Local Group* ,
Annual Review of Astronomy and Astrophysics, Volume 36, 1998, pp. 435-506, (1998). Link

[28] Matthew G. Walker, Mario Mateo and Edward W. Olszewski,
*Stellar Velocities in the Carina, Fornax, Sculptor and Sextans dSph Galaxies: Data from the Magellan/MMFS Survey*,
The Astronomical Journal, 137, 3100-3108, (2008). Link

[29] Matthew G. Walker,
*Dark Matter in the Milky Way's Dwarf Spheroidal Satellites*,
arXiv:1205.0311 2 May 2012. Link

[30] Max Tegmark, Michael A. Strauss and Michael R. Blanton,
*Cosmological parameters from SDSS and WMAP*,
Physical Review D 69, 103501, 5 May 2004 Link

[31] Maxwell Moe, Kaitlin M. Kratter and Carles Badenes,
*The Close Binary Fraction of Solar-type Stars Is Strongly Anticorrelated with Metallicity*,
The Astrophysicial Journal, 875:61, 2019 April 10. Link

[32] Meguin E. Spencer, Mario Mateo et al. ,
*The Binary Fraction of Stars in Dwarfs Galaxies: The Case of LeoII*,
AJ, Vol. 153, Number 6, 254 (2017). Link

[33] Meguin E. Spencer, Mario Mateo et al. ,
*The Binary Fraction of Stars in Dwarf Galaxies: the Cases of Draco and Ursa Minor*,
The Astronomical Journal, 156-257, 2018 December. Link

[34] Michael Marks and Pavel Kroupa,
*Dynamical population synthesis: constructing the stellar single and binary contents of galactic field populations*,
Mon. Not. R. Astronomic Society 417, 1702-1714 (2011). Link

[35] N. Ivanova, K. Belczynski, J. M. Fregeau et al,
*The evolution of binary fractions in globular clusters*,
Monthly Notices of the Royal AStronomical Society, Volume 358 issue 2, April 2005. Link

[36] Pavel Kroupa, Christopher A. Tout and Gerard Gilmore
*The low-luminosity stellar mass function*,
Mon. Not, R. Astronomic Society, 244, 76-85 (1990). Link

[37] Quinn E. Minor,
*Binary Populations in Milky Way Satellite Galaxies: Constrains From Multi-Epoch Data in the Carina, Fornax, Sculptor, and Sextans Dwarf Spheroidal Galaxies* ,
The Astrophysicial Journal, 779:166 (18pp), (2013 December 20). Link

[38] Ralf S. Klessen and Pavel Kroupa. ,
*Dwarf spheroidal satellite galaxies without dark matter: Results from two different numerical techniques*,
The Astronomical Journal, 1998 May . 498: 143-155. Link

[39] Robert W. Slawson, Andrej Prsa et al. ,
*Kepler eclipsing binary stars. II. 2165 eclipsing binaries in the second data release*,
The Astrophysicial Journal, 2011 November 142-160. Link

[40] Robin M. Green,
*Spherical Astronomy*,
Cambridge University press 1985.

[41] S. C. Madden, A. Rém-Ruyer et al. ,
*An Overview of the Dwarf Galaxy Survey* ,
The Astronomical Society of the Pacific, 2013 June . 125: 600-635. Link

[42] S. Paul, R. S. John et al. ,
*Understanding 'galaxy groups' as a unique structure in the universe*,
Monthly Notices of the Royal Astronomiclas Society MNRAS 471, 2-11, 2017. Link

[43] Shapley, H ,
*A Stellar System of a New Type*,
Harvard College Observatory, Bulletin 908, 1. March 1, 1938. Link

[44] Sidney van den Bergh ,
*The local group of galaxies* ,
Annual Review of AStronomy and Astrophysicis. 1999. 9: 273-318. Link

[45] Sidney van den Bergh ,
*Udated Information on the local Group* ,
The Astronomical Society of the Pacific, 2000 April . 112: 529-536. Link

[46] Siramas Komonjinda,
*A study of binary star orbits using precise radial velocity measurements with the HERCULES spectrograph*,
University of Canterbury, PHD, 2008. Link

[47] T. J. L. de Boer, E. Tolstoy, V. Hill et al,
*The star formation and chemical evolution history of the sculptor dwarf spheroidal galaxy*,
Astronomy and Astrophysics 539, A103 (2012). Link

[48] T. Hettinger, C. Badenes, J. Strader et al. ,
*Statistical time-resolved spectroscopy: A higher fraction of short-period binaries for metal-rich F-type dwarfs in SDSS*,
The Astrophysical Journal Letters, Volume 806, Issue 1, article id. L2, 5 pp. (2015).Link

[49] Tamman, G. A. 1994, in European Southern Observatory Conf. Workshop Proc, eds. G Meylan, & P. Prugniel, 49, 3.

[50] V. A. Ambartsumian,
*On the statistics of double stars*,
Astronomical Zhurnal 14 , 207, (1937). Link

[51] William Herschel,
*Catalogue of 500 New Nebulae, Nebulous Stars, Planetary Nebulae, and Clusters of Stars; With Remarks on the Construction of the Heavens*,
Philosophical Transactions of the Royal Society of London, vol. 92, The Royal Society, 1802, pp. 477–528. Link

[52] Wikimedia commons. LinkFig.1 LinkFig.20

[53] Xiaoan Wu,
*The mass distribution of dwarf spheroidal galaxies from stellar kinematics: Draco, Ursa Minor and Fornax*,
arXiv:astro-ph/07022334 (2007). Link